Monthly Notices of the ROYAL ASTRONOMICAL SOCIETY

MNRAS **543,** 3172–3195 (2025) https://doi.org/10.1093/mnras/staf1620
Advance Access publication 2025 September 25

JADES NIRSpec spectroscopy of GN-z11: evidence for Wolf–Rayet contribution to stellar populations at 430 Myr after big bang?

M. L. P. Gunawardhana [1,2,3★] J. Brinchmann [4,5] S. Croom [1] A. J. Bunker,[6] J. Bryant[1] and S. Oh [7]

[1]*Sydney Institute for Astronomy (SIfA), School of Physics, The University of Sydney, Sydney, NSW 2006, Australia*
[2]*Siding Spring Observatory, Research School of Astronomy and Astrophysics, Australian National University, Canberra, ACT 2611, Australia*
[3]*ASTRO 3D: ARC Centre of Excellence for All Sky Astrophysics in 3 Dimensions, Australia*
[4]*Instituto de Astrofísica e Ciências do Espaço, Universidade do Porto, CAUP, Rua das Estrelas, PT4150-762 Porto, Portugal*
[5]*Departamento de Fśica e Astronomia, Faculdade de Ciências, Universidade do Porto, Rua do Campo Alegre 687, PT4169-007 Porto, Portugal*
[6]*Department of Physics, University of Oxford, Denys Wilkinson Building, Keble Road, Oxford OX1 3RH, UK*
[7]*Department of Astronomy and Yonsei University Observatory, Yonsei University, Seoul, 03722, Republic of Korea*

Accepted 2025 September 12. Received 2025 August 26; in original form 2025 March 26

ABSTRACT

We investigate the unusual emission-line luminosity ratios observed in the JWST Deep Extragalactic Survey (JADES) NIRSpec spectroscopy of GN-z11, which reveal exceptionally strong emission lines and a significant detection of the rarely observed N III] $\lambda 1748-1753$, multiplet. These features suggest an elevated N/O abundance, challenging existing models of stellar populations and nebular emission. To assess whether Wolf–Rayet (WR) stars can account for the observed line ratios, we construct a suite of stellar and nebular models incorporating high-resolution stellar spectral libraries, enabling a more accurate treatment of WR evolution and its influence on the ionizing radiation field. We find that the inclusion of WR stars is essential for reproducing the observed position of GN-z11 in the C III]/He II versus C III]/C IV diagnostic plane, resolving discrepancies from previous studies. The model-derived metallicity ($0.07 \lesssim Z/Z_{\odot} \lesssim 0.15$), ionization parameter ($\log U \approx -2$), and stellar ages are consistent with the literature estimates. However, our models underpredict the N III/O III] ratio, suggesting that WR stars alone cannot fully explain the nitrogen enrichment. This suggests that additional mechanisms, such as rapid chemical enrichment in a young, metal-poor environment, may be necessary to explain the nitrogen excess. While our models successfully reproduce most observed line ratios, further refinements to the models are needed to fully characterize the stellar populations and the enrichment processes of high-redshift galaxies like GN-z11.

Key words: galaxies: abundances – galaxies: evolution – galaxies: high-redshift – galaxies: starburst – galaxies: stellar content.

1 INTRODUCTION

Since its first light, the *James Webb Space Telescope* (*JWST*) has revolutionized our understanding of the early Universe, probing deeper than ever before and challenging existing models of galaxy formation and evolution at cosmic dawn. One of the remarkable discoveries facilitated by *JWST* is GN-z11, the most luminous galaxy candidate at $z > 10$ in the Great Observatories Origins Deep Survey (GOODS) North field (R. J. Bouwens et al. 2010; P. A. Oesch et al. 2016). At just ~ 430 Myr after the big bang, GN-z11 offers a unique, yet puzzling, glimpse into the astrophysical processes driving the emergence of the first generations of galaxies. Intriguingly, its spectrum from *JWST*-NIRSpec (A. J. Bunker et al. 2023) reveals extreme ultraviolet (UV) and optical emission lines, including the rarely observed N III]$\lambda\lambda$1748-1753, along with [C III], C III] $\lambda\lambda$1907, 1909, C IV $\lambda\lambda$1548, 1550, and He II λ1640emission features.

The analysis of A. J. Bunker et al. (2023) highlights that GN-z11 occupies unique regions of emission-line diagnostic diagrams, driven in part by its unusually high nitrogen-to-oxygen (N/O) abundance ratio, pose a challenge to the existing photoionization models for both active galactic nuclei (AGNs) and starburst galaxies (e.g. A. Feltre, S. Charlot & J. Gutkin 2016; J. Gutkin, S. Charlot & G. Bruzual 2016). This raises critical questions about the chemical enrichment processes occurring in galaxies at such an early epoch.

The origin of GN-z11's extreme line luminosities and high N/O abundance remains a topic of active debate. While various physical mechanisms have been proposed to explain the unusual properties of GN-z11, its true nature remains elusive.

For instance, A. J. Cameron et al. (2023) explore several scenarios to explain the unusually high nitrogen enrichment observed in GN-z11. Their study concludes that while conventional stellar evolution models struggle to account for the elevated N/O ratio, alternative mechanisms – such as Wolf–Rayet (WR) stars, runaway stellar collisions in dense clusters facilitating the formation of very massive stars, and tidal disruption events – may provide more viable explanations. Further evidence supporting the presence of very massive stars in GN-z11 is presented by J. S. Vink (2024), who propose that stars with initial masses between 100 and 1000 $M_{\odot}$ are key

★ E-mail: madusha.gunawardhana@sydney.edu.au

contributors to nitrogen enrichment in star-forming (SF) galaxies. Due to their proximity to the Eddington limit, these massive stars undergo substantial mass loss via powerful stellar winds, enriching the surrounding interstellar medium (ISM) with nitrogen. While J. S. Vink (2024) assigns less weight to the WR scenario in GN-z11, a recent study by K. Watanabe et al. (2024) incorporating chemical evolution models with yields from various supernova types, like core-collapse supernovae, Type Ia supernovae, hypernovae, and pair-instability supernovae, suggests that these mechanisms alone do not fully account for the high N/O ratio. Instead, nitrogen enrichment may be attributed to winds from rotating WR stars that undergo direct collapse.

On the other hand, R. Maiolino et al. (2024) highlight the detection of [Ne IV] λ2453, and C II*λ1335 transitions, both of which are commonly associated with AGN activity, along with the detection of semiforbidden nebular emission lines, suggestive of high-density gas, to argue for the presence of an AGN in GN-z11. In contrast, P. Senchyna et al. (2024) compare GN-z11's spectrum to local UV data sets and note similarities with Mrk 996, where a high concentration of WR stars and their CNO-processed ejecta produce a UV spectrum that closely resembles that of GN-z11. Based on detailed nebular modelling, P. Senchyna et al. (2024) suggest the peculiar nitrogenic features prominent in GN-z11 may be a unique signature of intense and densely clustered star formation, potentially linked to the evolutionary precursors of present-day globular clusters.

Further support for the AGN hypothesis comes from J. Scholtz et al. (2024). They report extended Lyα emission located SW of GN-z11's continuum centre, and an extended C III] λ1909 emission in the same direction (R. Maiolino et al. 2024), which they interpreted as evidence of an AGN-driven ionization cone.

Conversely, several studies provide evidence supporting the starburst nature of GN-z11. For instance, J. Álvarez-Márquez et al. (2025) utilize deep medium-resolution spectroscopy from JWST's Mid-Infrared Instrument (MIRI) covering the rest-frame optical spectrum of GN-z11 to model its Hα and O IIIλ5008 emission features. They find the line profiles to be well represented by a narrow Gaussian component, with no indication of a dominant broad Hα emission line typically associated with the broad-line region of an AGN, though they do not entirely rule out the possibility of a weak-line AGN contribution. Taking into account the high star formation rate and stellar mass surface densities of GN-z11, J. Álvarez-Márquez et al. (2025) propose that the galaxy is undergoing a highly efficient starburst phase.

Similar conclusions are drawn in the model-based studies of C. Kobayashi & A. Ferrara (2024), C. Nagele & H. Umeda (2023), and F. Rizzuti et al. (2025). For instance, C. Kobayashi & A. Ferrara (2024) propose an intermittent star formation scenario, where a quiescent phase lasting 100 Myr separates two starbursts. They find that the emergence of WR stars immediately following the second starburst can account for the elevated N/O abundance observed in GN-z11. Similarly, C. Nagele & H. Umeda (2023) use simulations to suggest that metal-enriched supermassive stars, evolving shortly after the zero-age main sequence, could produce supersolar nitrogen levels consistent with the observations of GN-z11. Finally, F. Rizzuti et al. (2025) employ chemical evolutionary models incorporating various star formation histories (SFHs) to demonstrate that galaxies with extreme star formation rates and differential galactic winds – where the products of core-collapse supernovae are preferentially expelled – can achieve supersolar N/O abundances.

Building on the work of A. J. Bunker et al. (2023), our study in the current paper leverages *JWST* observations of GN-z11 to investigate the physical properties of its stellar populations, ionizing sources, and chemical enrichment. Using the updated stellar population synthesis (SPS) code, STARBURST99, which incorporates the latest WR classifications, accurate massive stellar evolution, updated isochrones, and high-resolution stellar and WR libraries that more uniformly sample the effective temperature, surface gravity, and stellar rotation parameter space of high-mass stars, alongside photoionization modelling (CLOUDY), we investigate the potential contributions of massive WR stars to the extreme ionizing radiation in GN-z11. We also explore mechanisms that could explain the elevated N/O abundance, aiming to bridge the gaps in our understanding of GN-z11's unique emission properties, as well as building upon previous efforts in modelling starburst regions using self-consistent approaches to accurately reproduce both stellar and nebular properties (e.g. J. M. Gomes & P. Papaderos 2017; M. L. P. Gunawardhana et al. 2020).

The paper is structured in two main parts. In the first part, we introduce GN-z11 in Section 2, followed by a detailed description of the construction of a comprehensive stellar and nebular model library (Sections 3 and 4). This includes modelling starbursts across stellar metallicities that permit WR star formation, utilizing an updated STARBURST99 code (Section 3) coupled with the photoionization code CLOUDY (Section 4) to characterize both stellar populations and nebular properties in highly SF regions. The second part of the paper applies these models to investigate the stellar and nebular properties of GN-z11 within the framework of various UV diagnostic diagrams (Section 5).

The assumed cosmological parameters are $H_0 = 70\,\mathrm{km\,s^{-1}\,Mpc^{-1}}$, $\Omega_M = 0.3$, and $\Omega_\Lambda = 0.7$. We assume a P. Kroupa (2001) stellar initial mass function (IMF) with high-mass cut-off of 120 $M_\odot$ throughout.

2 JADES NIRSPEC SPECTROSCOPY OF GN-Z11

The NIRSpec observations of GN-z11, the most luminous candidate $z > 10$ Lyman break galaxy in the GOODS-North field, were taken as a part of the JWST Deep Extragalactic Survey (JADES) collaboration between the NIRSpec and NIRCam instrument science teams. This study uses the GN-z11 data set described in detail in A. J. Bunker et al. (2023).

Briefly, the GN-z11 was observed with high priority using NIRSpec in its microshutter array mode (P. Ferruit et al. 2022), comprising of four arrays of 365×171 independently operable shutters, with 98 arcsec × 91 arcsec sky coverage. Our study uses the co-added data, with a total integration time of 3.45 h in each medium-resolution ($R \approx 1000$) *G140M/F070LP* (0.70–1.27 μm), *G235M/F170LP* (1.66–3.07 μm), and *G395M/F290LP* (2.87–5.10 μm) grating, and 6.9 h in the low-resolution ($R \approx 100$) PRISM/CLEAR mode (0.7–5.3 μm). The observations were processed with the reduction pipelines developed by the NIRSpec instrument science and GTO teams (A. J. Cameron et al. 2023). Based on the processed data, A. J. Bunker et al. (2023) report a redshift of 10.6034 ± 0.0013 for GN-z11.

For the analysis presented in this paper, we use the medium-resolution GN-z11 spectra presented in fig. B.1 of A. J. Bunker et al. (2023).

In the subsequent sections, we present and discuss the development of the suite of high-resolution and self-consistent stellar and nebular models, and their application to interpret the NIRSpec observations of GN-z11.

3 STELLAR POPULATION SYNTHESIS MODELLING

The *JWST* has significantly expanded our ability to probe much higher redshifts, allowing the observations of young, massive stellar

populations that emit a substantial portion of their flux in the far-UV. The increasing number of distant galaxy observations has intensified the need to improve SPS models, facilitating more reliable interpretations of these galaxies' physical properties (C. M. Byrne & E. R. Stanway 2023; C. Pacifici et al. 2023). However, a major challenge in studying high-redshift stellar populations using evolutionary population synthesis is the limited availability of comprehensive, high-resolution models with extended UV wavelength coverage. In this section, we detail our approach to incorporating theoretical stellar spectral libraries, aiming to model both the stellar and nebular features of young, massive stellar populations in a self-consistent manner. This approach leverages the spectral resolution and wavelength range provided by *JWST*-NIRSpec spectroscopy.

To generate high-resolution stellar population templates, we use the STARBURST99 code of C. Leitherer et al. (1999), which has been modified to model more accurately the key evolutionary phases of massive stars. The subsequent sections detail the modifications to the three core components of SPS models. In Section 3.1, we discuss the implementation of the stellar isochrones used in this study, which map a star's position in the bolometric luminosity–effective temperature plane (or equivalently, in the surface gravity–effective temperature plane) based on its mass, initial chemical composition, and age. The incorporation of the high-resolution stellar libraries, including WR stars, tracing different evolutionary stages of stars (A. Vazdekis et al. 2012), is detailed in Sections 3.2 and 3.3. Finally, in Section 4, we describe the self-consistent construction of nebular models using the CLOUDY photoionization code of G. J. Ferland et al. (2013), integrating the updated STARBURST99 SPS models as input.

3.1 The stellar evolutionary models

For the analysis presented in this paper, we utilize two widely used single-stellar evolutionary models; the GENEVA high mass-loss models (G. Schaller et al. 1992; C. Charbonnel et al. 1993; G. Meynet et al. 1994) and the PARSEC models (A. Bressan et al. 2012; Y. Chen et al. 2014, 2015). Recent models that have incorporated both rotational effects in massive stars (e.g. GENEVA and MESA Isochrones and Stellar Tracks; G. Meynet et al. 1994; B. Paxton et al. 2013) and binary evolution (e.g. BPASS; J. J. Eldridge & E. R. Stanway 2009; J. J. Eldridge et al. 2017; Y. Götberg et al. 2019) have also been published. Compared with single-evolutionary models, the models including stellar rotation and multiple stellar evolution tend to extend the effects of different evolutionary phases of massive stars.

While binary evolution effects offer a more complete picture of massive stellar evolution, the use of single-stellar evolutionary models in this study is both appropriate and advantageous. These models provide a well-controlled framework for isolating the impact of different evolutionary phases on spectral features. Their efficiency in exploring parameter space and fine-tuning model parameters makes them particularly well suited for this investigation.

Furthermore, although we have not explicitly accounted for stellar rotation in this study, we note that, within STARBURST99, the minimum stellar masses required for the onset of the WR phase are broadly comparable between the GENEVA high-mass-loss (HML) and rotational tracks. While rotational tracks are known to produce harder ionizing spectra and increased ionizing luminosities, much of these effects tend to be effectively captured by the GENEVA tracks through their HML prescriptions (J. Brinchmann, D. Kunth & F. Durret 2008b). As shown by C. Leitherer et al. (2014), rotation can enhance the ionizing photon output (e.g. a factor of 2–5 enhancement in the Lyman continuum for very young populations), however, these differences generally fall within the broader uncertainties associated with mass-loss calibrations. Likewise, S. Ekström et al. (2012) and J. Choi et al. (2016) highlight that, although rotation affects surface abundances and stellar lifetimes, its influence on the ionizing continuum, particularly during the WR phase, remains moderate and is often comparable to the effects of mass-loss prescriptions or binarity. Therefore, we expect the predicted observables not to differ substantially between rotating and non-rotating tracks.

3.1.1 GENEVA *stellar evolutionary tracks*

The 'GENEVA HML' isochrones (G. Meynet et al. 1994) are generally preferred over any isochrones with standard mass-loss rates (e.g. GENEVA and PADOVA standard tracks) for modelling starburst galaxies, as they more accurately reproduce observations of the WR phase, particularly for low-luminosity WR stars (e.g. J. Brinchmann, M. Pettini & S. Charlot 2008a; E. M. Levesque, L. J. Kewley & K. L. Larson 2010; N. Byler et al. 2017). These models adopt mass-loss rates approximately twice those of the 'standard' grid (C. Jager, H. Nieuwenhuijzen & K. A. van der Hucht 1988), providing a more reasonable approximation of mass loss for massive stars evolving into the WR phase. Mass-loss rates for WR stars of the nitrogen subclass with hydrogen-free (hereafter WNE or early-type WN), WR stars of the carbon subclass (hereafter WC), and WR stars of the oxygen subclass (hereafter WO) remain unchanged, except for the WR stars of the nitrogen subclass with a specified hydrogen mass fraction, hereafter late-type WN or WNL stars (G. Meynet et al. 1994).

In this analysis, we utilize the existing implementation of GENEVA HML isochrones within STARBURST99, covering the full range in available stellar metallicities (i.e. Z=0.001, 0.004, 0.008, 0.02, and 0.04), assuming the solar metallicity to be $Z_{\odot}$= 0.02. The upper initial stellar mass limit is set at 120 $M_{\odot}$, with lower mass cut-offs at 25, 20, 15, 15, and 12 $M_{\odot}$, respectively, from low-to-high stellar metallicity. The HML models as implemented in STARBURST99 are, therefore, combined with the 'standard' models to extend the stellar mass range down to 0.1 $M_{\odot}$, sampling around 22 different stellar mass values over 51 time intervals.

In the next section, we detail the implementation of the PARSEC isochrones in STARBURST99. A key difference between the GENEVA and PARSEC models lies in their treatment of mass-loss rates, which significantly influence the evolution of massive stars. We also examine how these variations in mass-loss rates affect the transition of massive stars into the WR phase across different metallicities in Section 3.3.1.

3.1.2 PARSEC *stellar evolutionary tracks*

In addition to the GENEVA models, we also utilize the PARSECv1.S isochrones[1] (A. Bressan et al. 2012; Y. Chen et al. 2014, 2015) for this analysis to investigate how the model assumptions change between the two sets of isochrones. The PARSEC tracks are calculated for a scaled-solar composition, with the initial helium content linked to the initial metallicities by the relation $Y_i = 1.78 \times Z_i + 0.2485$, assuming a solar metallicity of $Z_{\odot}$=0.0152.

The PARSEC release spans a broad range of metallicities, from 0.0001 to 0.04, with initial masses up to 350 $M_{\odot}$, and sample finely in stellar mass. It includes improvements in the treatment of boundary conditions for low-mass stars (Y. Chen et al. 2014, $\sim$ 0.6 $M_{\odot}$), as

[1]The PARSECv1.2S library is downloaded from the CMD3.1 web interphase (http://stev.oapd.inaf.it/cgi-bin/cmd)

well as updates to envelope overshooting and up-to-date mass-loss rates for massive stars (J. Tang et al. 2014; Y. Chen et al. 2015, i.e. $14 \lesssim M/M_{\odot} \lesssim 350$).

We generate isochrones using evolutionary tracks from the PARSECv1.S library for integration into STARBURST99. These tracks take advantage of fine sampling across time, metallicity, and stellar mass, encompassing 52 distinct stellar masses in the range $0.1 \lesssim M/M_{\odot} \lesssim 350$. Each evolutionary track is sampled non-uniformly at 1000 time-steps to capture all stellar evolutionary phases, and cover the evolutionary stage from very near the zero-age main sequence (Y. Chen et al. 2015) to the end stages for massive stars, or up to 10 Gyr for low-mass stars.

To accurately model the critical WR phase of massive stars, we apply corrections to the effective temperatures of all PARSECv1.S evolutionary models of massive stars. The derivation and justification of these temperature adjustments are discussed in Section 3.3.

3.2 The stellar spectral library

There are several approaches to producing stellar libraries for SPS codes, each with its own strengths and limitations. For generating SPS models in SF regions, one critical requirement is comprehensive coverage of the effective temperature ($T_{\rm eff}$), surface gravity ($\log g$), and metallicity ([Fe/H]) parameter space. Additionally, extended wavelength coverage is essential, as different stellar phases peak at different wavelengths.

Empirical stellar libraries, though valuable for being based on observed stellar spectra, are still constrained by the availability of stars within the Galaxy. Ongoing and completed observational campaigns (e.g. J. S. Vink et al. 2023; J. M. Bestenlehner et al. 2025) have continued to expand the coverage of massive stars, however, empirical libraries remain limited in their ability to fully sample the parameter space, particularly for rare, high-mass stars. Consequently, for this analysis, we choose theoretical stellar libraries as they provide a more comprehensive framework for modelling young, massive stellar populations. These theoretical spectra are generated using radiative transfer processes to simulate flux from model stellar atmospheres (R. L. Kurucz 1992; U. Munari et al. 2005), enabling coverage across the entire Hertzsprung–Russell (HR) diagram, exploring all possible atmospheric parameters.

One of the main drawbacks of theoretical libraries is their dependence on tabulated opacities and atomic/molecular absorption strengths, which can have significant uncertainties. Despite these challenges, accurately modelling young, massive stellar populations requires a stellar spectral library that covers the full parameter space of $T_{\rm eff}$, $\log g$, and [Fe/H], along with extended wavelength coverage. In this context, theoretical libraries remain the best option for capturing the evolution of high-mass stars across the desired parameter space.

We integrate the synthetic ultraviolet-blue (UVBLUE) library of L. H. Rodríguez-Merino et al. (2005) into STARBURST99 to meet the high spectral resolution requirements in the UV regime. The UVBLUE library, calculated at a resolution of 50 000 using the ATLAS9 and SYNTHE codes of R. Kurucz (1993), consists of 1770 spectra covering a wavelength range of 850–4700 Å. The grid spans 3000–50 000 K in effective temperature, $0.0 - 5.0$ in log surface gravity at steps of $+0.5$ dex, and includes seven metallicities ([M/H] $= -2.0, -1.5, -1.0, -0.5, +0.0, +0.3$, and $+0.5$ dex). The synthetic spectra assume solar-scaled abundances from N. Grevesse & A. J. Sauval (1998) and employ the atomic and diatomic molecular line lists of R. L. Kurucz (1992).

The diatomic molecular lines included in the computation are C_2, CN, CO, H_2, SiO, CH, NH, OH, MgH, and SiH, excluding TiO lines for cooler stars and atomic lines with theoretical transitions (i.e. 'predicted' lines). While uncertainties in the wavelengths and intensities of these predicted lines can introduce spurious absorption features and contaminate high-resolution spectra (U. Munari et al. 2005; P. Coelho et al. 2007), flux calibration remains essential for any high-resolution spectral library used to derive broad-band colours, as the absence of predicted lines can otherwise lead to inaccuracies in colour predictions. As the present study focuses on exploring the evolutionary phases of massive stars, and as we do not intend to use the current library for broad-band colour determinations, the uncertainties arising from the lack of predicted lines are expected to be relatively low.

3.3 The Wolf–Rayet spectral library

We combine STARBURST99's low-resolution CMFGEN library (D. J. Hillier & D. L. Miller 1998) with the higher-resolution Potsdam grids[2] of model atmospheres for WR stars (Galactic; Large Magellanic Cloud, LMC; Small Magellanic Cloud, SMC; and sub-SMC), developed by W.-R. Hamann & G. Gräfener (2004); A. Sander, W.-R. Hamann & H. Todt (2012); and H. Todt et al. (2015). The Potsdam Wolf–Rayet (PoWR) library provides extensive grids of expanding, non-local thermodynamic equilibrium, iron-group line-blanketed atmospheres for WR subtypes: WN stars, characterized by strong helium and nitrogen lines, and WC stars, defined by strong helium and carbon lines. The inclusion of iron-group line blanketing is crucial for accurately reproducing the observed spectra of WR stars, particularly WC subtypes, where numerous iron line transitions (Fe IV, Fe V, and Fe VI) form a pseudo-continuum in the UV that dominates the spectral energy distribution (SED; G. Gräfener, L. Koesterke & W.-R. Hamann 2002).

The PoWR grids are parametrized by luminosity (L^*), effective temperature ($T_{\rm eff}$), and wind density. The WR stars exhibit wind densities that are typically an order of magnitude higher than those of O-type stars, which are thought to be the result of multiple-photon scattering events due to their high luminosity-to-mass ratios (P. A. Crowther 2007; C. Leitherer et al. 2014). The strong, broad emission features characteristic of WR stellar spectra originate in their powerful stellar winds, forming far from the stellar surface. This increase in the optical thickness in mass-loss ($\dot{M}$) winds significantly impacts WR star modelling. For instance, at a given metallicity, the minimum stellar mass required for a massive star to enter the WR phase decreases with higher $\dot{M}$, while the WR phase duration increases. Additionally, both the time spent in each WR subtype and the surface composition are highly sensitive to mass-loss rates (G. Meynet et al. 1994).

Moreover, the optical thickness and strength of WR winds influence the hardness of their ionizing radiation, redistributing extreme UV photons toward redder wavelengths. As a result, WR stars appear cooler and larger in size than they would in the absence of mass loss. Therefore, the shape of the ionizing flux distribution, particularly the transparency below 228 Å contributing to He^0 ionizing photons, of WR stars is a strong function of both the wind density and $T_{\rm eff}$ (N. Langer 1989; P. A. Crowther 2007).

Given the non-negligible role of wind density in determining the features of WR stars, the PoWR library of WN and WC grids are

[2]The Potsdam grids (http://www.astro.physik.uni-potsdam.de/~wrh/PoWR/powrgrid1.php) cover wavelengths > 950 Å.

defined as a function of wind density, parametrized in terms of a 'transformed radius' (W. Schmutz, W. R. Hamann & U. Wessolowski 1989, R_T), and $T_{\rm eff}$. To integrate the PoWR library into STARBURST99, we adopt the approach of C. Leitherer et al. (2014), employing the parametrization established by W. Schmutz et al. (1989) as,

$$R_T = R_*\left(\frac{v_\infty}{2500}\Big/\frac{\sqrt{D}\dot{M}}{1\times10^{-4}}\right)^{2/3}, \quad (1)$$

where R_* is the effective stellar radius in the unit of m, v_∞ is the terminal wind velocity in the unit of km s^{-1}, and $\dot{M}$ is the mass-loss rate in M$_\odot$ yr^{-1}. Based on the observational evidence of line profile variabilities (A. F. J. Moffat et al. 1988) and the overprediction of the amplitude of the scattering wings in theoretical line profiles (D. J. Hillier 1991), the winds of WR stars are thought to be clumped (G. Gräfener et al. 2017; L. Grassitelli et al. 2018). Therefore, the wind clumping factor, D, acts to downward revise $\dot{M}$, although the exact amount is unclear (L. J. Smith, R. P. F. Norris & P. A. Crowther 2002), for the present study, we adopt the typical values of D in the literature (e.g. L. Dessart et al. 2000; P. A. Crowther et al. 2002; L. J. Smith et al. 2002; P. A. Crowther 2007; E. I. Doran et al. 2013; R. Hainich et al. 2014; C. Leitherer et al. 2014) in the range $4-10$ for WC stars to ~ 4 for WN subtypes (P. A. Crowther 2007).

Under the W. Schmutz et al. (1989) definition of R_T, for a given $T_{\rm eff}$ and metallicity, the model spectra with the same R_T have approximately the same emission-line equivalent widths regardless other specific wind parameters (H. Todt et al. 2015), meaning that for a fixed luminosity, the model depends only on R_T and $T_{\rm eff}$.

3.3.1 *Linking WR atmospheres with stellar evolutionary tracks*

The challenge of integrating WR atmospheres with stellar evolutionary models is a complex and long-standing problem in SPS. This problem exists because the optical thickness of WR stellar winds causes the observed radiation to emerge at larger radii. Consequently, the observed temperatures of WR stars cannot be directly linked to the hydrostatic core temperatures ($T_{\rm hyd}$) provided by evolutionary models without an inward extrapolation (W. Schmutz et al. 1989; L. J. Smith et al. 2002).

To this end, A. Maeder (1990); G. Meynet et al. (1994); and G. A. Vázquez et al. (2007) propose a potential solution, suggesting the use of a velocity law to estimate an effective radius corresponding to an optical depth (τ) of $\frac{2}{3}$. This approach allows the hydrostatic core temperature to be scaled to the temperature at this optical depth ($T_{2/3}$). However, as noted by W. Schmutz, C. Leitherer & R. Gruenwald (1992) and L. J. Smith et al. (2002), the $T_{2/3}$ derived from WR atmospheres typically remain around 30 000 K across different WR subtypes, and still lower than $T_{\rm hyd}$ predicted by evolutionary models.

To address this discrepancy, we adopt a hybrid approach, as detailed below.

Following A. Maeder (1990); G. Meynet et al. (1994); G. Meynet & A. Maeder (2005); and G. A. Vázquez et al. (2007), we assume the effective radius at a $\tau \approx 2/3$ is related to the classical photospheric radius (R$_{\rm hyd}$) via,

$$R_{2/3} = R_{\rm hyd} + \frac{3\kappa|\dot{M}|}{8\pi v_\infty}, \quad (2)$$

where κ is the opacity, and $|\dot{M}|$ is the mass-loss rate in M$_\odot$ yr^{-1}. Then using the Stefan–Bolzmann law, and assuming $L \approx L_{2/3}$, $T_{2/3}$ is calculated.

The challenge, then, is how to determine an accurate temperature for WR stars, given that $T_{\rm hyd}$ is generally too-high, while $T_{2/3}$ is typically too low. To address this, we adopt the weighted mean temperature approach proposed by L. J. Smith et al. (2002), which is based on analysing the distribution of WR temperatures from STARBURST99 at solar metallicity. In this formalism, the WR temperature ($T_{\rm WR}$) is defined as,

$$T_{\rm WR} = 0.6\times T_{\rm hyd} + 0.4\times T_{2/3}. \quad (3)$$

The formalism in equation (3) is used in correcting the temperatures during the WR phase only (G. A. Vázquez et al. 2007; C. Leitherer et al. 2014).

3.3.2 *The Wolf–Rayet stellar classification*

To become a classical WR star, a massive star must meet specific criteria for initial mass, $T_{\rm eff}$, and surface abundances of hydrogen (H), carbon (C), nitrogen (N), and oxygen (O). The minimum mass threshold, $M_{\rm min}$, is metallicity-dependent, increasing as metallicity decreases, while $T_{\rm eff}$ and surface abundances are dictated by the isochrones. According to single-star evolutionary theories, a star with an initial mass of $M_{\rm min}$ of 20 M$_\odot$ at solar metallicity can become a late-type WN star if its surface hydrogen fraction drops below 0.4 and $T_{\rm eff}$ exceeds 25 000 K. At the same metallicity, a higher $M_{\rm min}$ is required for the star to evolve into an early-type WN or a WC star (C. Georgy et al. 2012, 2015).

While the observational criteria for identifying WR stars are well established (P. A. Crowther 2007), classifying WR subtypes along a stellar evolutionary track of a given star is more challenging. There are several WR classification schemes exist in the literature, (e.g. C. Leitherer et al. 1999; C. Georgy et al. 2012; Y. Chen et al. 2015). In this study, we adopt a scheme similar to C. Georgy et al. (2012) and C. Leitherer et al. (1999) – a star is considered capable of entering the late-type WN phase if its zero-age main-sequence mass exceeds $M_{\rm min}$ for the given metallicity, its $T_{\rm eff}$ exceeds 25 000 K, and its surface H-abundance falls below 0.4. A star with negligible surface H-mass fraction and a C-to-N abundance ratio less than 1 while maintaining the $T_{\rm eff}$ requirement is classified as an early-type WN star. If the C-abundance $\geq$ N-abundance, the star is classified as a WC or WO subtype. We further differentiate between WC and WO subtypes based on the surface abundance ratio of C+O to helium.

In Fig. 1, we illustrate the evolution of WR spectra for a 120 M$_\odot$ star as it enters the WR phase, sampled in steps of 0.1 Myr. Each panel, from left-to-right, and top-to-bottom, shows the complete PoWR library grids for WNE, WNL-H20,[3] and WC subtypes at solar, LMC, SMC, and sub-SMC metallicities, respectively. The colour coding and the contours represent the stellar photospheric temperatures at specified $T_{\rm WR}$ and R_T.

As discussed earlier, we apply a correction to the stellar effective temperatures of massive stars in the PARSEC stellar isochrones during their WR phases. In Fig. 1, the dashed lines illustrate how WR spectral selection varies depending on whether $T_{\rm hyd}$ (black-dashed), $T_{2/3}$ (red-dashed), or $T_{\rm WR}$ (blue-dashed) is used. The need for this temperature correction is especially evident in the selection of WNL stars, where $T_{\rm hyd}$ is overestimated for WNL WR-subtype at solar, LMC, and SMC metallicities (i.e. $T_{\rm hyd}$ extends to beyond the PoWR grids towards higher $T_{\rm WR}$), while $T_{2/3}$ tends to be underestimated. The weighted mean temperature correction generally aligns WR temperatures to be within the respective PoWR grids. The correction, however, remains inadequate for the SMC grid, where all selections

[3]For this study, we select the PoWR grid for the WR stars of the nitrogen subclass with 20 per cent hydrogen mass fraction, i.e. WNL-H20.

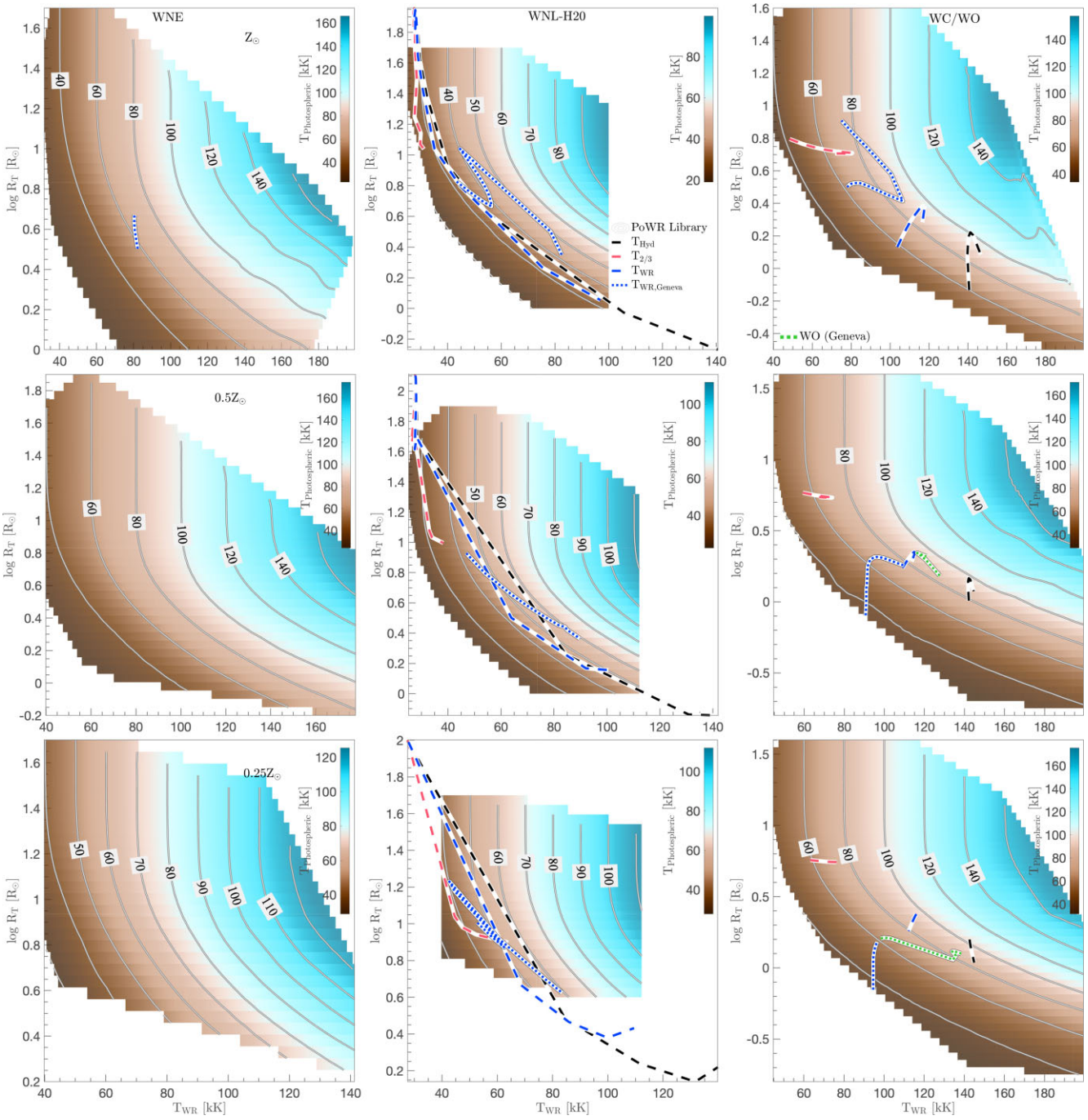

Figure 1. On the selection of WR spectra as a function of $T_{\rm WR}$ [10^3 K] and $R_{\rm T}$ [$R_\odot$] for PARSEC and GENEVA stellar isochrones from PoWR library. The panels (left-to-right, top-to-bottom) show PoWR grids for WNE, WNL-H20, and WC spectra at solar, LMC-like, SMC-like, and sub-SMC-like (∼0.7 Z⊙) metallicities. The contours and colour gradients represent photospheric temperatures as a function of $T_{\rm WR}$ and $R_{\rm T}$. Overlaid on each grid are evolutionary tracks for a 120 $M_\odot$ star from PARSEC (dashed) and GENEVA (dotted) isochrones as it enters its WR phase. For the PARSEC models, we show the selection of WR spectra with respect to $T_{\rm hyd}$ (black-dashed), $T_{2/3}$ (red-dashed), and $T_{\rm WR}$ (blue-dashed), and their respective $R_{\rm T}$s discussion in Section 3.3. For the GENEVA models, we only show the selection for $T_{\rm WR}$. Note that the panels displaying only the PoWR model grids indicate metallicities where PARSEC or GENEVA models do not predict the formation of WR stars. The green dotted lines indicate the WO evolutionary phase, which appears only in the GENEVA models for 120 $M_\odot$ stars. For this phase to occur in PARSEC models require higher stellar masses. The selection of WR spectra as a function of $T_{\rm WR}$ [10^3 K] and $R_{\rm T}$ [$R_\odot$] for PARSEC and GENEVA stellar isochrones from PoWR library for the sub-SMC-like (∼0.7 Z⊙) stellar metallicity.

extend beyond the PoWR grids at the lower temperature end. Note that the temperature corrections would be tapering off at the lower temperatures, as the primary goal is to address overly high temperatures.

Fig. 1 also shows the WNE (left column of panels), WC and WO (right column of panels) selections guided by the respective isochrones. Since the PoWR library lacks a separate WR spectral grid for WO subtypes, we substitute WC spectra in the population

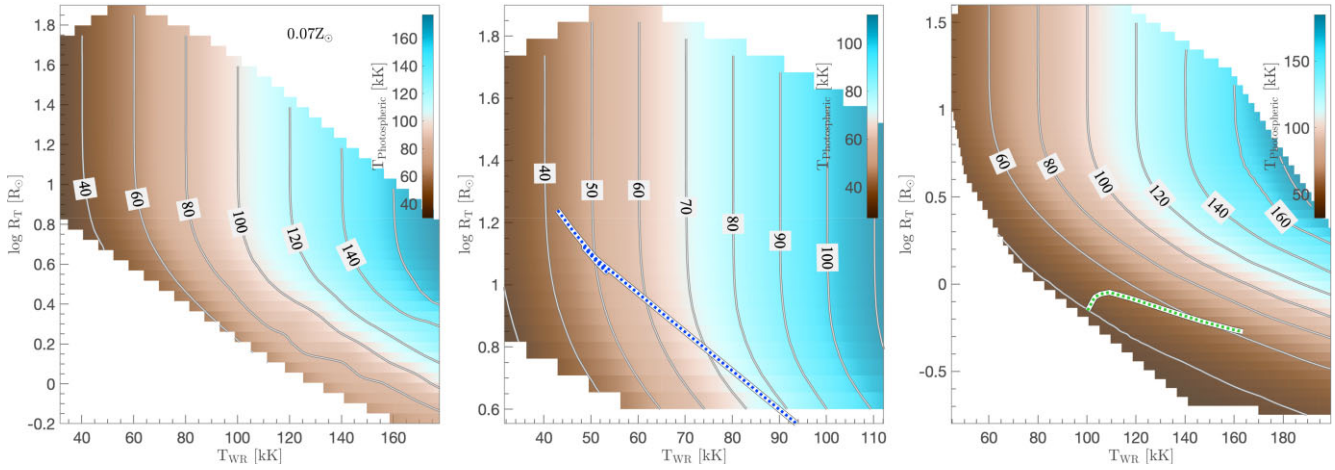

Figure 1. *Continued.*

synthesis analysis. Notably, no WR evolution is observed at sub-SMC metallicities with PARSEC isochrones, as they do not allow a 120 $M_\odot$ star to meet the conditions necessary to evolve into the WR phase.

In the same figure, we also present WR spectral selections based on GENEVA HML isochrones (dotted lines). The GENEVA isochrones already incorporate a temperature correction for WR stars, so we rely on their provided corrections to estimate the weighted mean temperatures shown in Fig. 1. One key difference between PARSEC and GENEVA isochrones is that GENEVA allows massive stars to achieve WR conditions at metallicities lower than that permitted by the PARSEC isochrones (see the bottom panels of Fig. 1). This discrepancy is mainly due to the higher mass-loss rates in the GENEVA models. These higher mass-loss rates at given metallicity enable massive stars to enter the WR phase at earlier stages of evolution compared to PARSEC. Consequently, at a given age, the higher mass losses allow more low-mass stars (with $M > M_{\rm min}$) to enter the WR phase with GENEVA than with PARSEC. Overall, achieving WR star formation at sub-SMC and lower metallicities typically requires high mass-loss rates or binary interactions.

Finally, since the PoWR grids begin at a wavelength of 950 Å, we supplement the spectra at shorter wavelengths by integrating them with the low-resolution CMFGEN library available in STARBURST99 (D. J. Hillier & D. L. Miller 1998), selecting models based on the closest matching $T_{\rm eff}$. Some of the enhancements to the modelling of WR features in the optical, achieved through the incorporation of high-resolution spectral libraries, are discussed in M. L. P. Gunawardhana et al. (2020).

4 PHOTOIONIZATION MODELLING

Predicting the ionizing spectrum is crucial for modelling young, massive stellar populations in SF regions. These spectra are typically dominated by a combination of nebular continuum, strong emission lines, and broad emission features characteristic of WR stars during intense starbursts. Accurate modelling of these strong nebular emissions is essential when comparing SPS models to observations of young stellar populations. In contrast, nebular emissions can generally be disregarded when modelling older stellar populations.

In this analysis, we generate photoionization models using version 23.00 of the CLOUDY code (M. Chatzikos et al. 2023) in a self-consistent manner, using the latest STARBURST99 templates as input. Version 23.00 of CLOUDY introduces substantial updates to atomic and molecular data, significantly enhancing the accuracy of its predictions. Notable improvements include the integration of the Chianti atomic database (version 10), updated collisional rates for H- and He-like ions, incorporation of the latest molecular data from the Leiden Atomic and Molecular Database (LAMDA; F. van der Tak et al. 2020), and revised chemical reaction rates for selected species.

For the gas-phase chemical composition, we adopt the 30-element abundance prescription from J. Gutkin et al. (2016), which primarily assumes solar-scaled abundances compiled by A. Bressan et al. (2012), except for a few elements.

In this framework, the solar (photospheric) metallicity is $Z_\odot = 0.01524$, consistent with the PARSECV1.S isochrones. J. Gutkin et al. (2016) also fine-tuned the solar oxygen and nitrogen abundances from A. Bressan et al. (2012) to better match the observed properties of Sloan Digital Sky Survey (SDSS) galaxies in several optical diagnostic diagrams. For non-solar metallicities, the abundances of primary nucleosynthesis elements are assumed to scale linearly with the ISM metallicity.

Nitrogen, being both a primary[4] and secondary[5] nucleosynthesis element, requires special treatment. As a secondary nucleosynthesis element, its abundance is expected to scale with stellar metallicity (J. Gutkin et al. 2016). To relate the primary+secondary N-abundance to O, we use the relationship proposed by B. A. Groves, M. A. Dopita & R. S. Sutherland (2004) and adopted by J. Gutkin et al. (2016). Additionally, we assume a solar C/O ratio of $(\rm C/O)_\odot = 0.44$.

To account for the depletion of refractory metals onto dust grains, we also adopt the ISM depletion factors from J. Gutkin et al. (2016). The metals depleted from the gas phase contribute to grain formation, which significantly affects the scattering and absorption of incident radiation, radiation pressure, collisional cooling, and photoelectric heating of the gas. Depleting key cooling agents from the gas phase reduces gas cooling efficiency, thus increasing the electron temperature and, thereby, enhancing cooling through more energetic optical transitions (M. A. Dopita et al. 2002; B. A. Groves et al. 2004; J. Gutkin et al. 2016). The extent of metal depletion is characterized

[4]Nitrogen is synthesized as a primary element in CNO cycles during the Hydrogen-burning of stars in the $4 \lesssim M/\rm M_\odot \lesssim 8$.

[5]Nitrogen is also synthesized as secondary nucleosynthesis element from CO products of previous generations of stellar populations (M. A. Dopita et al. 2000; J. Gutkin et al. 2016)

Table 1. Grid sampling of the main parameters of the photoionization model library.

Parameter	Sampled range
Ages (Myr)	0.2–500 Myr[a] (94 different values)
Stellar metallicity	$0.001 - Z_{\odot}$[b] (5 different values)
IMF upper mass cut ($M_{\odot}$)	120
Gas metallicity	$0.001 - Z_{\odot}$[c] (5 different values)
$n_{\rm H}$ (cm^{-3})	100, 500, 1000[c]
Burst strengths (log $M_{\odot}$)	$2 - 5$[d]

Notes. [a] The ages are variably sampled. In the models, the young ages (i.e. < 10 Myr) are sampled at 0.1 Myr steps in order to fully capture the evolutionary effects of massive stars, particularly the effects of the crucial short-lived WR phase. The ages in the range $\sim 10 - 100$ Myr sampled at steps of 10 Myr, and the $100 - 500$ Myr in steps of 100 Myr.
[b] The present day (photospheric) solar metallicity (Z_s) is assumed to be $Z_{\odot} = 0.0152$, matching with PARSEC isochrones and J. Gutkin et al. (2016) abundances. Note that the solar metallicity assumed for the GENEVA isochrones is 0.02.
[c] We assume $Z_{\rm ISM}$=Z_s (i.e. gas-phase metallicities are assumed to be equal to stellar metallicity).
[d] Any range of burst strengths can be assumed provided the corresponding evolution of $\log U$ is in the $-0.5 \lesssim \log U \lesssim 4$ range. We assume a fixed radius for our model H II regions. For an H II region of a different radius, these strengths need to be scaled following equation (4).

by the gas-to-metal mass fraction, ξ_d. Following J. Gutkin et al. (2016), we adopt $\xi_d = 0.36$, indicating that 36 per cent of heavy elements by mass are locked in dust grains.

While ξ_d is inherently metallicity-dependent, in this study, we assume a constant ξ_d across all metallicities. Since we focus only on metallicities capable of producing WR stars, the uncertainties introduced by this assumption are relatively minor, and we discuss its implications for model predictions and comparisons in Section 5.3.

For constructing the CLOUDY models of SF regions, we assume a simple spherical geometry. While not entirely realistic, the studies of SF regions dominated by young, massive stars and their birth clouds find a spherical approximation to be sufficient (e.g. A. Efstathiou, M. Rowan-Robinson & R. Siebenmorgen 2000; R. Siebenmorgen & E. Krügel 2007). Additionally, we use emission-line luminosity ratios throughout this study to minimize the impact of the underlying assumption of a spherical geometry.

4.1 Grid of CLOUDY photoionization models

This section outlines the development of a comprehensive suite of photoionization models designed to investigate the UV emission-line properties of SF galaxies.

In CLOUDY modelling, the ionization parameter, U, determines the intensity of the ionizing continuum, and depends on the number of ionizing photons ($Q_{\rm H}$), which characterizes the strength of a starburst, and hydrogen density ($n_{\rm H}$). U is defined as,

$$U = \frac{Q_{\rm H}}{4\pi R^2 \times n_{\rm H} \times c}, \tag{4}$$

where c is the speed of light and R is the radius of the ionized region, assumed to be fixed at 3 pc. While we fix the radius for our model H II regions, the radius can be varied posteriori, permitting starbursts of any magnitude to be generated provided the U range probed is within the range of input to CLOUDY.

Table 1 summarizes the sampling of key model parameters considered in this study. For a single stellar generation, most ionizing photons are emitted within the first 10 Myr, during which the effects of WR stars are also most pronounced. Therefore, we sample younger ages (< 10 Myr) at a finer time resolution of 0.1 Myr, while the gas density $n_{\rm H}$ is sampled at a coarser resolution to establish lower and upper bounds for the model grid. Throughout this analysis, we assume that gas-phase metallicity ($Z_{\rm ISM}$) matches the stellar metallicity.

The most common diagnostics for characterizing the nature of nebular excitation are the BPT diagnostics (J. A. Baldwin, M. M. Phillips & R. Terlevich 1981). As a preliminary check, before examining the UV emission-line properties, we assess the predicted behaviour of [O III] λ5007/Hβ and [N II] λ6584/Hα from our new model suite in Fig. 2.

Fig. 2(a) illustrates the evolution of the [O III] λ5007/Hβ ratio for starbursts of 1000 and 10 000 $M_{\odot}$, with $n_{\rm H} = 100$ and 1000 [cm^{-3}], assuming $Z_{\rm ISM} = Z = Z_{\odot}$. The grey shading indicates the period during which massive stars evolve into WR stars in a single stellar generation. As stars enter the WR phase, the ionizing continuum intensifies, leading to a sharp increase in the [O III] λ5007/Hβ ratio. Conversely, this ratio rapidly drops as massive stars exit the WR phase. The impact of $n_{\rm H}$ and starburst strength is minimal at earlier ages (< 6 Myr), while significant variations in the [O III] λ5007/Hβ ratio are observed at later ages (> 6 Myr), although these ratios are too low to be detectable in H II regions.

Figs 2(b) and (c) illustrate the evolution of [O III] λ5007/Hβ and [N II] λ6584/Hα for SMC, LMC, and solar metallicities, assuming a starburst of strength 10 000 $M_{\odot}$ and $n_{\rm H} = 100$ and 1000 [cm^{-3}]. The shaded region, the same as in Fig. 2(a), represents the ages where WR star effects become significant at for a $Z_{\rm ISM} = Z = Z_{\odot}$. As discussed in Section 3.3, both the onset and duration of the WR phase depend on mass-loss rates and metallicity. The $M_{\rm min}$ threshold for WR formation is lower at higher metallicities, allowing more low-mass stars to enter the WR phase than at low metallicities, thereby extending the duration of the influence of WR stars on the stellar population's evolution.

The impact of the metallicity dependence of ionizing photon from WR stars on BPT diagnostics is evident in panels (b) and (c), where the peak in [O III] λ5007/Hβ (and the decline in [N II] λ6584/Hα) occur at younger ages for higher metallicity models compared to subsolar models, reflecting the longer WR durations at higher metallicities. In contrast, the WR effects in subsolar models are less pronounced and taper off more gradually due to the higher $M_{\rm min}$ threshold, resulting in fewer massive stars entering the WR phase. Finally, increasing $n_{\rm H}$ enhances both [O III] λ5007/Hβ and [N II] λ6584/Hα due to a higher rate of collisional excitation.

Figs 2(d) and (e) present the BPT diagnostic plots. Like Fig. 2(a), Fig. 2(d) focuses exclusively on solar metallicity models, allowing us to distinguish the effects of varying burst strengths and $n_{\rm H}$ values at a fixed radius. The blue and brown solid lines represent the evolution of BPT diagnostics for starbursts of 1000 and 10 000 $M_{\odot}$, respectively, with the darker and lighter shades of each colour denoting $n_{\rm H} = 100$ and 1000 [cm^{-3}], respectively. The black solid and dashed lines denote the demarcations from L. J. Kewley et al. (2001) and G. Kauffmann et al. (2003), separating AGNs from SF galaxies and composites, and pure SF systems, respectively. The dashed grey line represents the best fit to the low-redshift SDSS data from J. Brinchmann et al. (2008a).

As the starburst strength is defined by $Q_{\rm H}$ (equation 4), an increase in $Q_{\rm H}$ will, in turn, increase U, extending the evolutionary tracks towards higher [O III] λ5007/Hβ and lower [N II] λ6584/Hα regime in the BPT plane. Conversely, for a given $Q_{\rm H}$, an increase in $n_{\rm H}$ will lower U, thus shifting the evolutionary tracks towards higher [N II] λ6584/Hα.

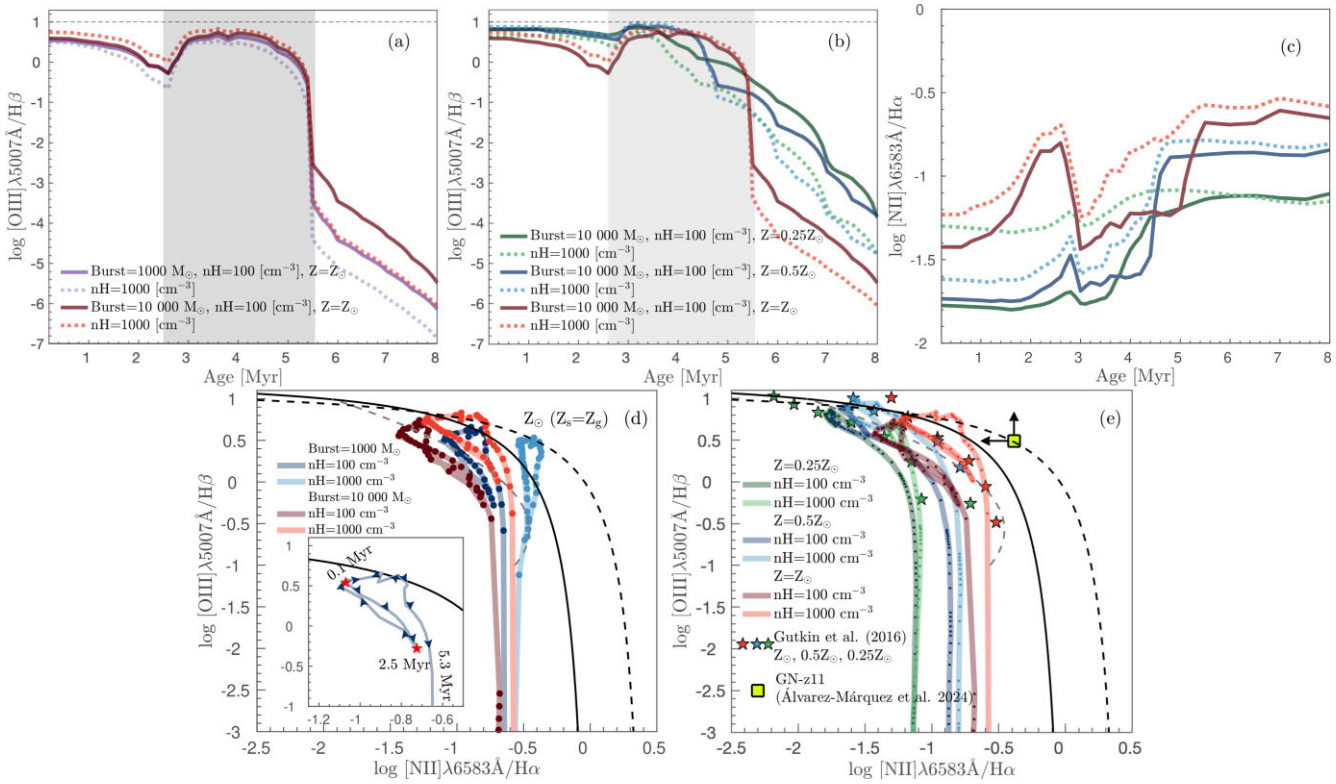

Figure 2. The behaviour of the predicted nebular lines used in BPT diagnostics (J. A. Baldwin et al. 1981). (a) The evolution of [O III] λ5007/Hβ line luminosity ratio as a function of $n_{\rm H}$ (solid and dotted lines) at solar metallicity ($Z_{\rm s}$=$Z_{\rm g}$) for bursts of star formation of strengths 1000 and 10 000 $M_\odot$ for a model H II region of a fixed radius. (b) and (c) show the evolution of [O III] λ5007/Hβ and [N II] λ6584/Hα as a function of $n_{\rm H}$ for SMC, LMC, and solar metallicities for a fixed starburst of 10 000 M⊙. The shaded regions in (a) and (b) show the timespan over which the WR phase is significant. The beginning and the duration of the WR phase of massive stars are largely functions of stellar metallicity. (d) demonstrates the predicted behaviour in the BPT diagram for starbursts of strengths 1000 and 10 000 $M_\odot$ for a solar stellar and gas metallicity. For each burst, we plot two $n_{\rm H}$ values (100 and 1000 cm^{-3}), shown as darker and lighter shades, respectively. The black dashed and solid lines show the L. J. Kewley et al. (2001) and G. Kauffmann et al. (2003) demarcations, respectively, and the dashed grey line denotes the fit to the SDSS data from J. Brinchmann et al. (2008a). In the inset, we illustrate the general evolutionary behaviour of the tracks for solar metallicity. The two red stars denote the first age point (0.1 Myr) of the track and the age at which the WR stars first appear (2.5 Myr), with the arrows tracing the evolution of the line luminosities in the BPT plane. Finally, (e) shows the evolution in the BPT plane for SMC-, LMC-, and solar-like metallicities for a fixed burst strength of 10 000 $M_\odot$ and for two different $n_{\rm H}$ values. For comparison, we overplot the J. Gutkin et al. (2016) models for the same metallicities as stars. Also, overplotted in lime green is the *JWST*-MIRI spectroscopy-based optical line ratios for GN-z11 from J. Álvarez-Márquez et al. (2025), with arrows denoting the upper limits.

To illustrate the effects of WR stars on the evolution of BPT diagnostics, a zoomed-in view of the solar model is shown in the inset of Fig. 2(d). The red stars mark the start of the track and the age at which massive stars begin entering the WR phase, while the embedded arrows indicate the direction of evolution. Up to $\sim$ 2.5 Myr, the solar model evolves as expected, with the [O III] λ5007/Hβ gradually declining due to the aging of young, ionizing stars. At $\sim$ 2.5 Myr, however, the most massive stars start transitioning into the WR phase, and within $\lesssim$ 0.5 Myr, the hot, exposed cores of WR stars significantly boost the influx of ionizing photons, increasing U and inducing a rapid jump in [O III] λ5007/Hβ.

As the WR phase progresses, massive stars, from the most massive (i.e. 120 $M_\odot$) down to $M_{\rm min}$, gradually enter the WR phase. After the initial sharp increase in [O III] λ5007/Hβ, the ratio continues to rise, albeit at a slower pace, as additional stars evolve into WR stars. Similarly, [N II] λ6584/Hα ratio also shows an increase. The decline in [O III] λ5007/Hβ begins as massive stars start exiting the WR phase. As stars from 120 $M_\odot$ to $M_{\rm min}$ transition out of the WR phase, the [O III] λ5007/Hβ ratio shows an initial gradual decline, followed by a sharp drop, coinciding with the exit of all $>M_{\rm min}$ stars from the WR phase.

Fig. 2(e) presents the BPT diagrams for SMC (green), LMC (blue), and solar (red) models, assuming a burst strength of 10 000 $M_\odot$, and $n_{\rm H}$ = 100 and 1000 [cm^{-3}]. Notably, the enhanced influx of ionizing photons can propel the predicted line ratios into the composite (SF+AGN) regime. In higher metallicity models, the line ratios may even extend into the AGN region. We also overplot the J. Gutkin et al. (2016) models, spanning a similar metallicity range, in Fig. 2(e) to illustrate that our models are consistent with the literature.

Also overplotted in Fig. 2(e) is the GN-z11 BPT measurement based on *JWST*/MIRI medium-resolution spectroscopy (J. Álvarez-Márquez et al. 2025), with arrows indicating the upper limits of the measurements. The optical line ratios place GN-z11 within the composite region, suggesting contributions from both starburst activity and an AGN. According to J. Álvarez-Márquez et al. (2025), this is consistent with the properties of local low-metallicity starbursts and high-z luminous galaxies detected at similar redshifts to GN-z11. Notably, our starburst models exhibit a systematic shift towards the composite region as the electron density increases, particularly over the evolutionary phases where WR stars dominate. This trend suggests that our models will naturally encompass the observed position of GN-z11 on the BPT diagram at higher densities.

These excursions of the models shown in Figs 2(d) and (e) into the AGN/composite regime is primarily driven by the presence of the WR stars. In fact, a significant portion of the WR stellar phase of a stellar population is spent trekking towards and residing within this regime. This is particularly evident in solar models, where the WR effects are more pronounced.

Although we have not explicitly investigated this effect in our study, stochastic sampling of the stellar IMF can substantially broaden the dispersion of emission-line flux ratios in the BPT plane, particularly for starbursts with the strengths illustrated in Fig. 2. For instance, R. Orozco-Duarte et al. (2022) analyse a library of synthetic NUV, U, B, V, and I photometry for star clusters with stochastically sampled IMFs and ionized gas, covering cluster masses between 1000 and 10 000 $M_\odot$. They find that the largest photometric dispersion arises when WR stars are present, with nebular emission lines contributing over 50 per cent and 30 per cent of the total flux in the V and I bands, respectively. Similarly, R. Arora, M. R. Krumholz & C. Federrath (2021), using SLUG and CLOUDY simulations, quantify the uncertainties in H II region emission due to stochastic sampling. They demonstrate that stochasticity can introduce significant dispersion in emission-line ratios, especially at solar-like metallicities.

In the context of our results, the principal impact of stochastic sampling is to broaden the range of emission-line ratios sampled by a given model track. The magnitude of this broadening depends on metallicity, consistent with the metallicity sensitivity of massive star evolution to the WR phase. Based on the stochastic models of R. Arora et al. (2021), at solar metallicity, the broadening of tracks at fixed [O III]λ6584/Hα can exceed one magnitude, with the effect diminishing at lower metallicities.

4.1.1 On the excursions in the BPT plane – starburst strengths and durations based on sound-crossing time

To better understand the temporal nature of these excursions in the BPT plane, we analysis the likely sound-crossing times for different starbursts.

Star formation within a gaseous cloud can be triggered and propagated through various mechanisms. In this analysis, we consider a simplified model in which an external or internal perturbation propagates through the cloud, triggering star formation. The characteristic velocity at which information travels through the cloud is approximately set by the sound speed in the medium.

Assuming a cloud of roughly constant density, we can estimate its characteristic size based on its total mass. Dividing this size by the sound speed provides an approximate time-scale over which perturbations can traverse the cloud, triggering star formation.

Fig. 3 illustrates the sound crossing time as a function of $n_{\rm H}$ for different burst strengths, assuming a temperature of $T = 10^4$ K and a pure hydrogen composition. This simple analysis suggests that for starbursts with an average density of $n_{\rm H} = 10^3$ cm^{-3}, a typical duration of $\sim$1 Myr is a reasonable expectation. Several studies (e.g. R. Maiolino et al. 2024; P. Senchyna et al. 2024), however, highlight that the densities in GN-z11 can be higher than 10^3 cm^{-3}. As shown in Fig. 3, starburst durations of $\lesssim$1 Myr can be expected in such cases.

Assuming a starburst duration of $\sim$ 1 Myr, Fig. 4 presents the convolution of the two $n_{\rm H}$ models for a starburst of 1000 $M_\odot$ (indicated as solid lines and also shown in Fig. 2d) with a tophat function of 1 Myr duration. Given that GN-z11 is likely experiencing an extreme starburst, a 1 Myr smoothing time-scale is a realistic approximation

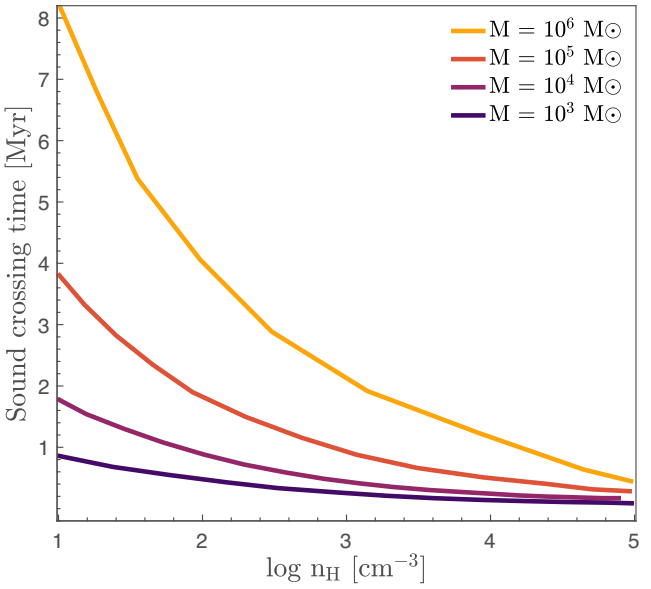

Figure 3. The sound-crossing time as a function of $n_{\rm H}$ for starbursts of different strengths.

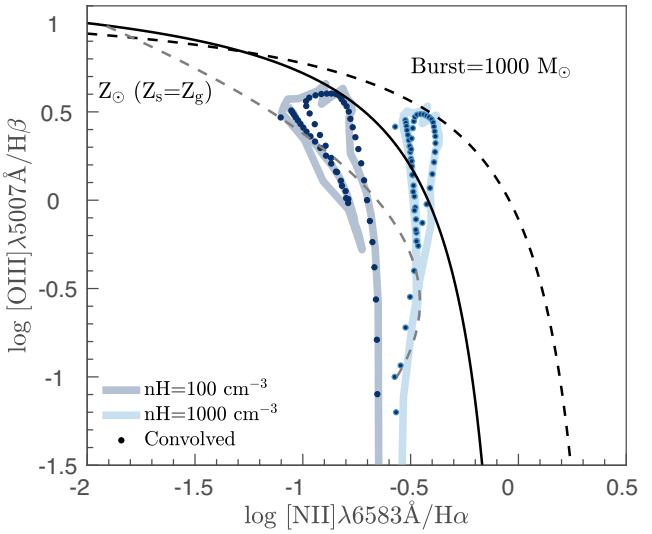

Figure 4. The model predictions for a starburst of 1000 M⊙ at solar metallicity, with nH values of 100 and 1000 cm^{-3} (solid lines, same as shown in Fig. 2), are compared with the same models convolved with a 1 Myr top-hat function (filled-in circles of the same colour). The convolution with the 1 Myr top-hat function demonstrates that the features in the models persist over longer time-scales.

of its starburst activity. The convolved models highlight that these excursions are not brief fluctuations but persist over sufficiently long time-scales to be observable in extreme starbursting environments.

Notably, starburst durations of $\lesssim$1 Myr, corresponding to $n_{\rm H} > 10^3$ cm^{-3} in GN-z11, as suggested by R. Maiolino et al. (2024) and P. Senchyna et al. (2024), would have even less minimal impact on the smoothing out fluctuations driven by WR populations observed in Fig. 2(d).

Furthermore, Figs 2(b) and (c) demonstrate that the interval between the emergence of the first WR stars and the disappearance of the last WR stars spans several million years across the metallicity

range studied, meaning that starbursting regions hosting WR stars can have emission-line ratio representative of AGN and composites.

In the following sections, we focus on model predictions in the UV regime for $Z \lesssim Z_{\odot}$, which is the primary focus of our study.

4.2 Ultraviolet emission-line properties

The diagnostics diagrams involving combinations of collisionally excited metal lines or line multiplets, such as N V λ1240 (multiplet), O I λ1304 (triplet), S IV λ1397+ O IV] λ1402, [N IV] λ1483+ N IV] λ1487 C IV λλ1548,1550, He II λ1640 (Balmer recombination line), O III] λλ1661,1666, N III λ1750 (multiplet), [C III] λ1907+ C III] λ1909, Si II λ1814 (multiplet), [Si III] λ1883+ Si III] λ1892, [O III] λ2321, [Ne IV] λ2424, [O II] λλ2470, 2471, [Ne III] λ3343, [Ne V]λ3426, [O II] λλ3726, 3729, and [Ne III] λ3868, are useful for identifying the nature of ionizing sources and constraining interstellar gas parameters and the shape of the ionizing radiation (B. A. Groves et al. 2004; A. Feltre et al. 2016). Most the lines listed above are detected in GN-z11. In addition, several higher order hydrogen Balmer lines, such as H5–H8, are also detected with high signal-to-noise ratio.

Among these, the collisionally excited C IV] λ1550 and C III] λ1909 are some of the most commonly detected UV emission lines in spectra (D. P. Stark et al. 2014, 2015). Together with the He II λ1640 Balmer recombination line, the diagnostics based on the C IV] λ1550 and C III] λ1909 offer better discrimination between AGN and shock-ionized gas than optical diagnostics, as these lines are predicted to be significantly stronger in shocks than in AGNs (M. Villar-Martin, C. Tadhunter & N. Clark 1997; M. G. Allen, M. A. Dopita & Z. I. Tsvetanov 1998; B. A. Groves et al. 2004).

In highly SF systems, however, the effects of massive stellar evolution must be considered when interpreting diagnostics involving C IV] λ1550 and C III] λ1909, and He II λ1640. At metallicities of $Z_{\rm ISM} > 0.006$, for instance, the nebular He II λ1640 can be affected by the broad stellar emission originating from WR stars, which are hotter, have denser winds, and are Helium enriched. Additionally, as metallicity increases, the number of energetic photons capable of producing nebular He II λ1640 drop, while stellar He II λ1640 emission rises due to an increase in the number of stars entering the WR phase, as the minimum mass required for WR formation decreases (G. Meynet 1995; R. Chandar, C. Leitherer & C. A. Tremonti 2004). The interpretation of C IV] λ1550 also presents challenges, as at $Z_{\rm ISM} > 0.006$, it can display P-Cygni absorption profiles due to the high mass-loss rates of O-type stars, which also depend on metallicity (N. R. Walborn & R. J. Panek 1984).

The ionizing photons in the Lyman continuum ($Q_{\rm H^0}$) are primarily produced by hot main-sequence stars, while WR stars contribute significantly to the He^0 and He^+ ionizing flux. In Fig. 5(a), we present the evolution of ionizing photon production [s^{-1}] over the $0.2 - 8$ [Myr] period, focusing on the ionizing continua for H^0 ($\lesssim 912$ Å), He^0 ($\lesssim 504$ Å), and He^+ ($\lesssim 228$ Å) at solar metallicity ($Z_{\odot}$ solid lines), half-solar metallicity ($0.5Z_{\odot}$ dotted lines), and quarter-solar metallicity ($0.25Z_{\odot}$ dashed lines). Subpanels (b) and (c) of Fig. 5 depict the hardness of the ionizing spectrum, expressed as the ratios of He^0 to H^0 ionizing luminosity and He^+ to H^0 ionizing luminosity, respectively, for the same metallicities shown in the main panel.

The most notable differences appear during the WR phase, from $\sim 2.5 - 6$ [Myr], particularly in the He^+ continuum ($\lesssim 228$ [Å], the upper edge of the He^+ ionizing region). These differences are primarily driven by the changing WR-to-O star ratio, with a higher proportion of stars entering the WR phase as metallicity increases. Furthermore, as metallicity rises, the He^+ continuum becomes increasingly sensitive to contributions from the various WR subtypes. This sensitivity manifests as the zig-zag pattern in Fig. 5(c), reflecting variations in the relative abundances of WR subtypes and O stars. Our models show broad agreement with those

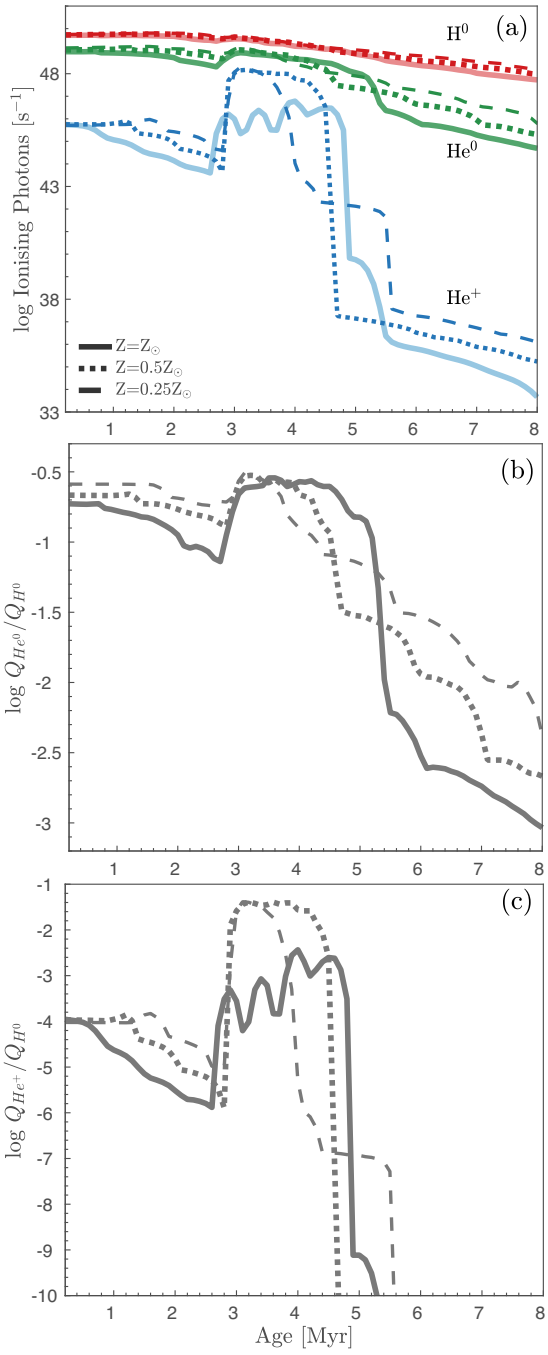

Figure 5. The evolution in ionizing luminosity and hardness of ionizing spectra. (a) The evolution of the number of ionizing photons (Q) for ages $\lesssim 10$ Myr in the ionizing continua of H^0 ($\lesssim 912$ Å), He^0 ($\lesssim 504$ Å), and He^+ ($\lesssim 228$ Å) at $Z_{\odot}$ (solid), $0.5Z_{\odot}$ (dotted), and $0.25Z_{\odot}$ (dashed) for a starburst of 1000 $M_{\odot}$ at time-steps of 0.1 Myr. In (b) and (c), the evolution of the hardness of ionizing spectra parametrized as $\log Q_{\rm He^0}/Q_{\rm H^0}$ and $\log Q_{\rm He^+}/Q_{\rm H^0}$, respectively.

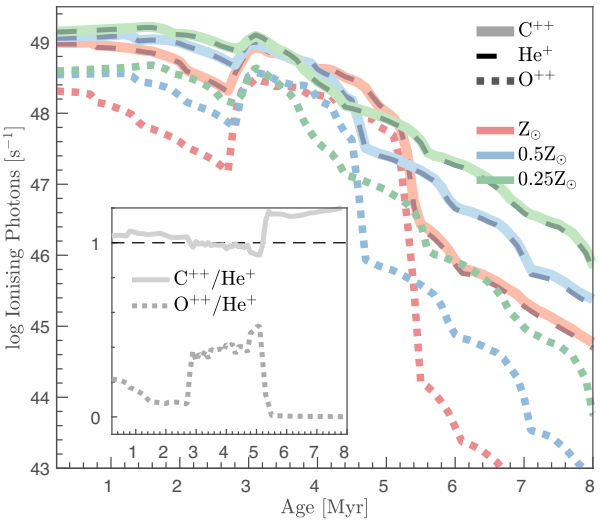

Figure 6. The evolution of the number of ionizing photons (Q) for ages $\lesssim$ 10 Myr in the ionizing continua of C^{++} (i.e. 258.9 $\lesssim \lambda$ [Å]$\lesssim$ 508.5), He^{+} (i.e. 504 $\lesssim \lambda$ [Å]$\lesssim$ 228), and O^{++} (i.e. 225.7 $\lesssim \lambda$ [Å]$\lesssim$ 353) species at $Z = Z_\odot$ (red), $0.5Z_\odot$ (blue), and $0.5Z_\odot$ (green) for a starburst of 1000 $M_\odot$ at time steps of 0.1 Myr. The inset presents the evolution of the ratio of C^{++} to He^{+} (solid line) and O^{++} to He^{+} (dotted lines), emphasizing, in particular, the differences in evolution between C^{++} and He^{+}, which appears as overlapping in the main plot.

of Charlot & Bruzual,[6] see Appendix A for a quantitative comparison and discussion of differences between the two model libraries.

Moreover, it is also important to note that the predicted ionizing fluxes and the hardness of the ionizing spectrum during the WR phase are highly sensitive to the adopted mass-loss prescriptions. Studies such as A. A. C. Sander, J. S. Vink & W. R. Hamann (2020) and F. Tramper, H. Sana & A. de Koter (2016) have shown that mass-loss rates scale strongly with parameters like the Eddington factor and metallicity, and likely also a function of WR subtypes. Enhanced mass loss increases wind opacity, which in turn suppresses the emission of He II ionizing photons and directly affects both the ionizing continuum and the spectral hardness. As a result, denser winds, particularly at high metallicity, tend to produce softer ionizing spectra.

In Fig. 6, we track the evolution of ionizing continuum for three higher ionization lines commonly observed in the UV spectra of SF galaxies: C^{++} (258.9 $\lesssim \lambda$ [Å]$\lesssim$ 508.5), He^{+} (504 $\lesssim \lambda$ [Å]$\lesssim$ 228) and O^{++} (225.7 $\lesssim \lambda$ [Å]$\lesssim$ 353) at $Z_\odot$, $0.5Z_\odot$, and $0.25Z_\odot$. The inset highlights the evolution of the ratios of C^{++}/He^{+} and O^{++}/He^{+}, offering a closer examination of the evolutionary trends seen in the main panel. While the C^{++} and He^{+} ionizing luminosities exhibit broadly similar patterns, the inset underscores the variations between the two, though they appear to be relatively subtle compared to O^{++}.

Model predictions for several commonly used UV diagnostics, which are also observed in the GN-z11 spectrum, are presented in Fig. 7.[7] The ratios C IV λλ1548, 1550, O IV] λ1666, and [C III], C III] λλ1907, 1909 with respect to He II λ1640 are shown in panels (a)–(c) of Fig. 7.

The ionization potentials of the species involved increase from C III (24.38 eV) to He II (24.59 eV), O III (35.12 eV), and C IV (47.89 eV) (C. Leitherer et al. 2011; C. C. Steidel et al. 2014; A. Feltre et al. 2016). Consequently, the number of photons energetic enough to produce higher ionization species decreases as the stellar population ages. This trend is particularly evident in panel (c), where the C III/He II ratio shows an increase at ages $\lesssim$ 2.5 [Myr] and $\gtrsim$ 6 [Myr], reflecting the relatively faster decline of He II ionizing photons compared to C III.

During the WR phase (∼2.5–6 Myr), the reverse occurs, with the C III/He II ratio showing a depression as He II ionizing photons are boosted by the hot, exposed cores of WR stars. The zig-zag pattern observed in the solar metallicity models is due to the sensitivity of the He^{+} ionizing flux to the WR subtype-to-O-star ratio, which becomes more pronounced at higher metallicities.

Both N IV] λλ1483, 1487 and N III] λ1747 − 1753 (multiplet 1747 $\leq \lambda \leq$ 1753 Å) are clearly detected in the GN-z11 NIRSpec/prism spectrum, implying extremely elevated nitrogen abundance in this system (A. J. Cameron et al. 2023). In Fig. 7(f), we show the evolutionary behaviours of nitrogen line luminosities with respect to oxygen. Finally, in Fig. 7(i), the ratio of the [O II] λλ3727, 3729, a well-known gas density diagnostic, is shown.

5 ON THE ANALYSIS OF JADES NIRSPEC SPECTROSCOPY OF GN-Z11

In this section, we focus on the disagreement between the measured GN-z11 flux ratios and the model predictions reported in A. J. Bunker et al. (2023). In their fig. 4, the observed flux ratio of GN-z11 is compared to the predicted [C III], C III] λλ1907, 1909/C IV λλ1548, 1550 versus [C III], C III] λλ1907, 1909/He II λ1640 diagnostics for SF galaxies (using the models of J. Gutkin et al. 2016) and AGNs (using the models of A. Feltre et al. 2016). These models consider metallicities in the range $0.066 \lesssim Z/Z_\odot \lesssim 0.131$ and hydrogen number densities $2 \lesssim \log n_H/\mathrm{cm}^{-3} \lesssim 4$, and A. J. Bunker et al. (2023) report that GN-z11 lies outside the parameter space sampled by either model set.

To explore this discrepancy, we replicate the diagnostic diagram from fig. 4 of A. J. Bunker et al. (2023), overlaying a subset of our models based on PARSEC stellar evolutionary tracks alongside the measured fluxes for GN-z11 (as reported in table 1 of A. J. Bunker et al. 2023). Fig. 8 shows the predicted [C III], C III] λλ1907, 1909 to C IV λλ1548, 1550 versus [C III], C III] λλ1907, 1909 to He II λ1640 nebular diagnostics for $Z/Z_\odot \gtrsim 0.25$, $2 \lesssim \log n_H \lesssim 4$, and a starburst of 10 000 $M_\odot$. The colour coding follows that of Fig. 7, and the shaded regions correspond approximately to the epochs dominated by WR star contributions for each respective metallicity.

The open blue rectangle highlights the parameter space sampled by starbursts with strengths of 1000 − 100 000 $M_\odot$ at $0.5Z_\odot$, while the orange data point represents the observed GN-z11 flux ratios (A. J. Bunker et al. 2023). For clarity, we only display models corresponding to solar metallicity as red circles. Additionally, in figures derived from PARSEC models, we restrict our focus to subsolar metallicities ($\gtrsim 0.25Z_\odot$) that still permit WR star formation. As noted earlier, of the subsolar metallicities explored in this study, $0.25Z_\odot$ is the lowest metallicity that allows WR star formation under PARSEC stellar evolutionary tracks. In contrast, GENEVA HML tracks enable WR star formation down to a metallicity of $0.07Z_\odot$.

The H II region models shown in Fig. 8 extend to overlap the GN-z11 data, in contrast to the J. Gutkin et al. (2016) models presented in fig. 4 of A. J. Bunker et al. (2023). This difference primarily arises

[6]The models can be downloaded from https://www.bruzual.org.

[7]For the remainder of this paper, we focus on models with solar and subsolar metallicities, excluding supersolar models.

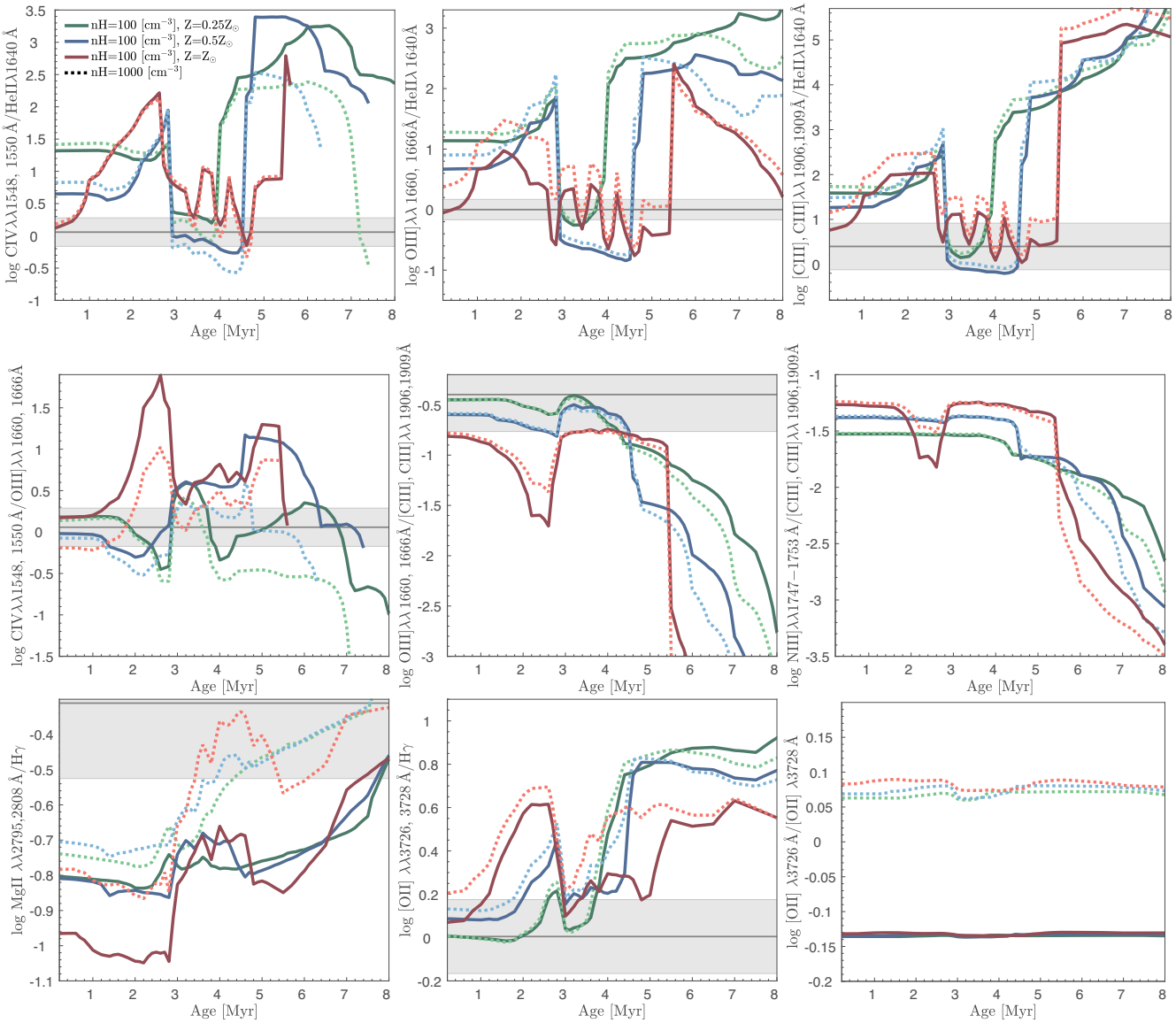

Figure 7. The evolution of different nebular emission-line luminosity ratios as a function of $n_{\rm H}$ and metallicity for a burst of star formation of strength 10 000 $M_\odot$ for a model H II region of a fixed radius. The evolutionary behaviour for $n_{\rm H} = 100$ (solid lines) and 1000 (dotted lines) [cm^{-3}], and $Z = Z_\odot$ to $0.25Z_\odot$ (different colours) are considered. The gas and stellar metallicities are assumed to be approximately similar. The observed line fluxes for GN-z11 reported by A. J. Bunker et al. (2023) are shown as a solid horizontal line with uncertainties represented by the shaded region for cases where the measurements exist and fall within the parameter space of the models.

from the distinct underlying assumptions between the two sets of models. The SF models of J. Gutkin et al. (2016) assume a continuous star formation rate of 1 $M_\odot$ yr^{-1} over 100 Myr, establishing a steady-state population of H II regions within a model galaxy before deriving predictions for nebular emission.

In contrast, our models track the evolution of a single stellar population, in which the majority of ionizing photons are produced during a period of < 10 Myr. This approach effectively captures the temporal evolution of an individual H II region following a burst of star formation. By comparison, the models of J. Gutkin et al. (2016) simulate ensembles of H II regions representative of an entire galaxy, thereby averaging over the distinctive features that may arise from a single, actively SF H II region.

Each approach has its advantages and limitations. Our single-burst approach allows for a detailed exploration of how different evolutionary stages of massive stars influence the behaviour of predicted emission-line luminosities, explicitly characterizing the evolution of massive stars within an H II region. On the other hand, the steady-state approach of J. Gutkin et al. (2016), which assumes ongoing star formation until 100 Myr, models a galaxy-scale population of H II regions. While GN-z11 is classified as a galaxy, our focus is on understanding the physical mechanisms – particularly the evolution of massive stars – that could produce the unusual line luminosities detected in its NIRSpec spectrum. To achieve this, tracing the impact of individual evolutionary phases of massive stars on the observed line luminosities requires studying a single starburst event.

As shown in Fig. 8, it is indeed possible to populate the region of the [C III], C III] λλ1907, 1909 to C IV λλ1548, 1550 versus [C III], C III] λλ1907, 1909 to He II λ1640 diagnostic plane at

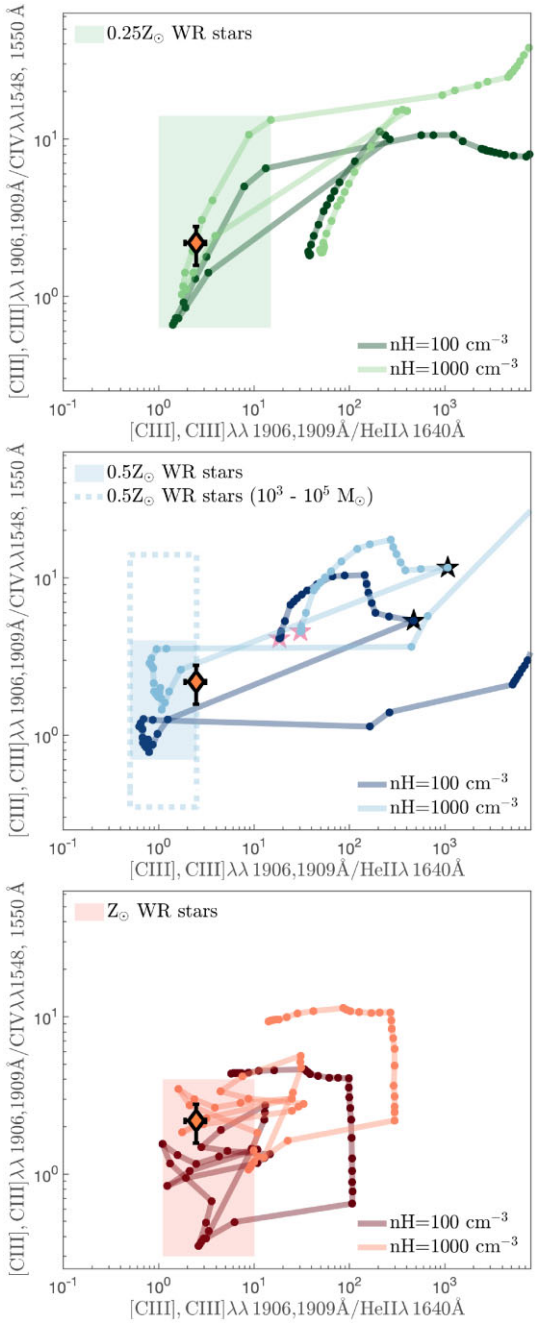

Figure 8. Predicted [C III], C III] λλ1907, 1909 to C IV λλ1548, 1550 versus [C III], C III] λλ1907, 1909 to He II λ1640 nebular emission-line ratios from our STARBURST99/PARSEC + CLOUDY models (equivalent to fig. 4 of A. J. Bunker et al. 2023) for a 10^4 $M_\odot$ starburst within a fixed-radius H II region. Panels (top-to-bottom) show subsolar to solar metallicities, respectively, with the observed GN-z11 line ratios from A. J. Bunker et al. (2023) indicated by orange diamonds. Top panel: the $0.25Z_\odot$ (SMC-like) models, with $n_H = 100\,cm^{-3}$ (dark lines) and $1000\,cm^{-3}$ (light lines). The shaded region indicate the parameter space sampled during the WR phase. Middle panel: the $0.5Z_\odot$ (LMC-like) models, with shaded region again marking the WR phase. The dashed rectangular region illustrates the additional parameter space covered when the starburst mass is varied between 10^3 and 10^5 $M_\odot$. The starting point of the evolutionary tracks (∼0.2 Myr) is marked by a red star, while the first appearance of WR stars is denoted by a black star. The terminal points of the tracks correspond to low log U values and generally fall outside the observable parameter space. Bottom panel: the $Z_\odot$ (MW-like) models, and the respective WR region.

the location of GN-z11 through contributions from WR stars.

In Fig. 9, we present our models' equivalent of fig. 8 from A. J. Bunker et al. (2023): the [Ne III] λ3869/[O II] λλ3726,3729 versus ([Ne III] λ3869+ [O II] λλ3726,3729)/Hδ diagnostic diagram, with the GN-z11 measurements overplotted as orange and cyan data points. Like oxygen, neon is a dominant ionizing species and a principal coolant in SF regions (K. Cunha, I. Hubeny & T. Lanz 2006). It is produced during the later stages of massive stellar evolution via carbon burning and is expected to closely track oxygen abundance in H II regions (E. M. Levesque & M. L. A. Richardson 2014).

The [Ne III] λ3869/[O II] λλ3726,3729 ratio effectively probes the the ionizing continuum shape (E. Pérez-Montero et al. 2007; E. M. Levesque & M. L. A. Richardson 2014) as the ionization thresholds of N^{++} (303 Å, ionization potential of 40.96 eV) and O^+ (911 Å, ionization potential of 13.62 eV) spans a wide UV wavelength range. This extended wavelength range provides greater sensitivity to shorter wavelengths, dominated by ionizing photons from young massive stars.

Similar to earlier figures, the evolutionary behaviour of [Ne III] λ3869/[O II] λλ3726,3729 versus ([Ne III] λ3869+ [O II] λλ3726,3729)/Hδ is shown in the left panel of Fig. 9 for $n_H = 100$ and 1000 [cm^{-3}], with starburst strengths of 10 000 (solid lines) and 100 000 $M_\odot$ (dotted lines). The inset in Fig. 9(b) provides a close-up of the evolution for the solar metallicity $n_H = 1000$ [cm^{-3}] model, emphasizing the behaviour of the predicted line ratios during the epochs dominated by WR stars when their ionizing flux contribution is most significant.

The right panel of Fig. 9 replots the same evolutionary tracks as the left panel but maps them to the ionization parameter range $-2.0 \lesssim \log U \lesssim -1.0$.

Our motivation for highlighting the parameter space sampled by models over $-2.0 \lesssim \log U \lesssim -1.0$ is to emphasize the Z–U dependence in our models, particularly since A. J. Bunker et al. (2023) report a $\log U$ of ~ -2.0 for GN-z11. Overall, our models within this ionization parameter range overlap with the GN-z11 measurements. While the 100 000 $M_\odot$ models show the best agreement with GN-z11, it is important to note that the ratio ([Ne III] λ3869+ [O II] λλ3726,3729)/Hδ can exhibit two solutions depending on metallicity. Specifically, for $Z/Z_\odot \lesssim 0.3$, the model tracks progressively shift toward higher ([Ne III] λ3869+ [O II] λλ3726,3729)/Hδ ratios with increasing metallicity, while for $Z/Z_\odot \gtrsim 0.3$, the trend reverses, shifting toward lower ratios.

The two solutions of ([Ne III] λ3869 + [O II] λλ3726,3729)/Hδ is partially evident in Fig. 9, where the $0.25Z_\odot$ models are sandwiched between the solar and $0.5Z_\odot$ models, though closer to the $0.5Z_\odot$ models, with some overlap likely resulting from differences in WR effects at varying metallicities.

Given the dependence of ([Ne III] λ3869 + [O II] λλ3726,3729)/Hδ on metallicity, it is possible that $Z/Z_\odot \lesssim 0.25$ models within $-2.0 \lesssim \log U \lesssim -1.0$, incorporating WR effects,[8] with moderate to high n_H values (∼1000 [cm^{-3}]), may provide better alignment with GN-z11. Finally, A. J. Bunker et al. (2023) report a metallicity range of $0.07 \lesssim Z/Z_\odot \lesssim 0.15$ for GN-z11, which is consistent with our findings.

[8]Recall that the PARSEC stellar evolutionary models do not allow WR star formation at $Z/Z_\odot \lesssim 0.25$, whereas GENEVA evolutionary models do.

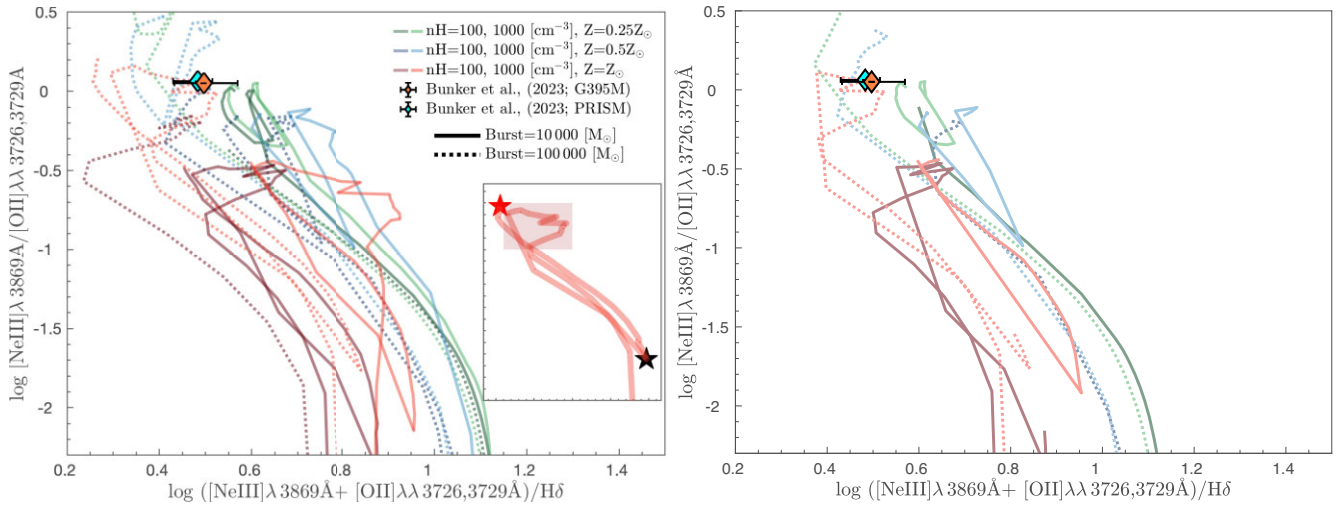

Figure 9. Our STARBURST99/PARSEC + CLOUDY models' equivalent of A. J. Bunker et al. (2023, figs 8; see also their comparison of GN-z11 with the J. Gutkin et al. 2016 models over the range $-4.0 \lesssim \log U \lesssim -1.0$). Left panel: the predicted evolution of [Ne III] λ3869/[O II] λλ3726,3729 versus ([Ne III] λ3869+ [O II] λλ3726,3729)/Hδ for bursts of star formation of strengths 10 000 and 100 000 $M_\odot$ (solid and dotted lines, respectively). The colour coding corresponds to different metallicities and is the same as in Fig. 8. The data points denote the line luminosity ratios reported in A. J. Bunker et al. (2023) based on *G*395*M* and PRISM/CLEAR observations. In the inset, we show the behaviour of the solar metallicity model, with the red and black stars indicating the start of the track and the point of the first appearance of WR stars. As in Fig. 8, the shaded region in the inset represents the parameter space the model points primarily occupy as massive stars starts to evolve in to WR stars. Right panel: same as in the left panel, except illustrating only the predictions in the $-2.0 \lesssim \log U \lesssim -1.0$.

5.1 The stellar populations in the GN-z11

For modelling the spectrum of an SF region rich in both stellar and emission features, a spectral fitting methodology that leverages the full range of nebular and stellar information to extract the SFH and physical properties is typically preferred (M. L. P. Gunawardhana et al. 2020). However, our study focuses on understanding the impact of the WR phase on nebular emission and stellar features. Accordingly, the STARBURST99 + CLOUDY model library we constructed is restricted to metallicities that permit WR star formation as dictated by the input stellar isochrones. Furthermore, throughout our analysis, we assume $Z = Z_{\rm ISM} = Z_s$.

We fit the STARBURST99 + CLOUDY models to the GN-z11 spectrum using model-fitting routines built on PLATEFIT, a code originally designed to perform non-negative least-squares fitting with dust attenuation treated as a free parameter, aiming to find the best-fitting stellar continuum model for a given spectrum (J. Brinchmann et al. 2004; C. A. Tremonti et al. 2004; M. L. P. Gunawardhana et al. 2020). To model the continuum, we combine stellar and nebular continua for a given stellar metallicity and treat dust attenuation as a free parameter using a simple attenuation curve, $\tau(\lambda) \propto \lambda^{-1.3}$, assuming similar extinction between young and old stellar populations. This exponent is suitable for describing the mid-range optical properties of dust grains between those of the Milky Way (MW), LMC, and SMC (S. Charlot & S. M. Fall 2000). Additionally, we find that the choice of alternative common attenuation laws in the literature (e.g. M. L. Prevot et al. 1984; D. Calzetti et al. 2000) has a minimal impact on the fitting results.

By design, PLATEFIT identifies the best-fitting stellar continuum model for a given spectrum. However, to address our aim of investigating the impact of WR stars, we extract the best-fitting linear combination of light-weighted models for each metallicity listed in Table 1. Since the input templates to PLATEFIT represent the evolution of a single stellar generation following a burst, our approach assumes that the SFH of GN-z11 can be approximated as a sum of discrete bursts for a given metallicity. The relative weights of individual models contributing to the SFH are defined relative to their luminosity at 2000 Å.

We combine the GN-z11 NIRSpec medium-resolution grating data from *G*140*M* (blue), *G*235*M* (green), and *G*395*M* (red) to perform PLATEFIT stellar and nebular continuum fitting as a function of Z_s. This process extracts the individual light-weighted stellar populations likely contributing to the SFH of GN-z11. We determine an approximate velocity dispersion during the continuum fitting, using trial velocity dispersions to converge on the value that minimizes the chi-squared statistic. The resulting best-fitting $Z = Z_\odot$ model is presented in Fig. 10, with grating data colour-coded as *G*140*M* (blue), *G*235*M* (green), and *G*395*M* (red).

The figure also compares the best-fitting model with (red) and without (blue) a correction for residuals to account for any subtle variations in the continuum, noting that the correction primarily affects the bluest and reddest regions of the spectrum. Overall, we find that the best-fitting model without additional residual corrections adequately represents the GN-z11 spectrum. The best-fitting continuum model is then subtracted to extract the nebular emission luminosities presented in Section 5.3.

Fig. 11 shows the individual light-weighted stellar and nebular continua templates contributing to the best-fitting $Z_s = Z_\odot$ model in Fig. 10. The youngest stellar templates, aged $3.1 - 3.5$ Myr, are shown in blue and contribute approximately over 50 per cent (by lightweight) to the total stellar population of GN-z11 at solar metallicity. The remaining contribution comes from a 10 Myr stellar population.

Prominent features in the youngest templates include broad emission peaks associated with WR stars and the Balmer Jump at 3645 Å, characteristic of young stellar populations.

Moreover, as previously discussed, we determine the best-fitting linear combination of stellar and nebular continuum models for all stellar metallicities that allow for WR star formation. The best-fitting models for $Z_s = 0.5$ and $0.25 Z_\odot$ assign similar weights to populations with ages of $\lesssim$3.5 Myr, with the remaining contribution distributed at

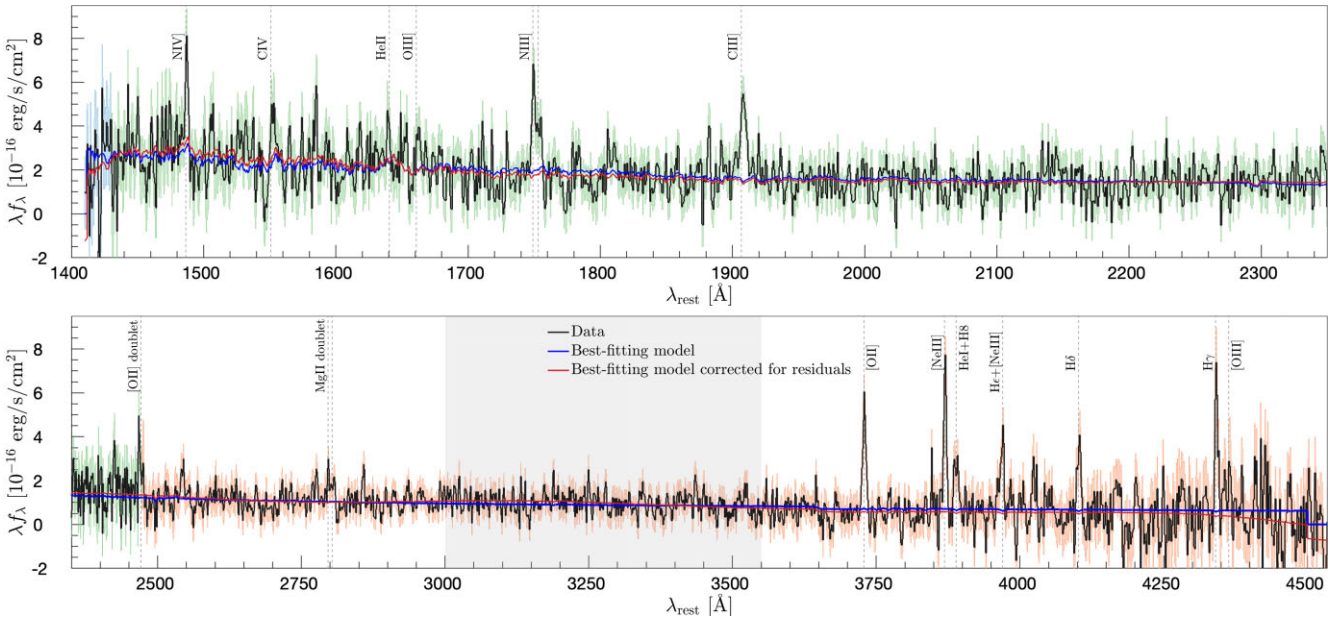

Figure 10. The best-fitting continuum model at $Z_s = Z_\odot$ with (blue solid line) and without (red solid line) a residual correction to GN-z11 medium resolution *G*140*M* (blue), *G*235*M* (green), and *G*395*M* (red) grating data shown in black. The prominent emission lines observed in the spectrum are labelled, with the grey-shaded region denoting the detection of continuum excess in the rest-frame UV between 3000 and 3550 Å reported by X. Ji et al. (2025).

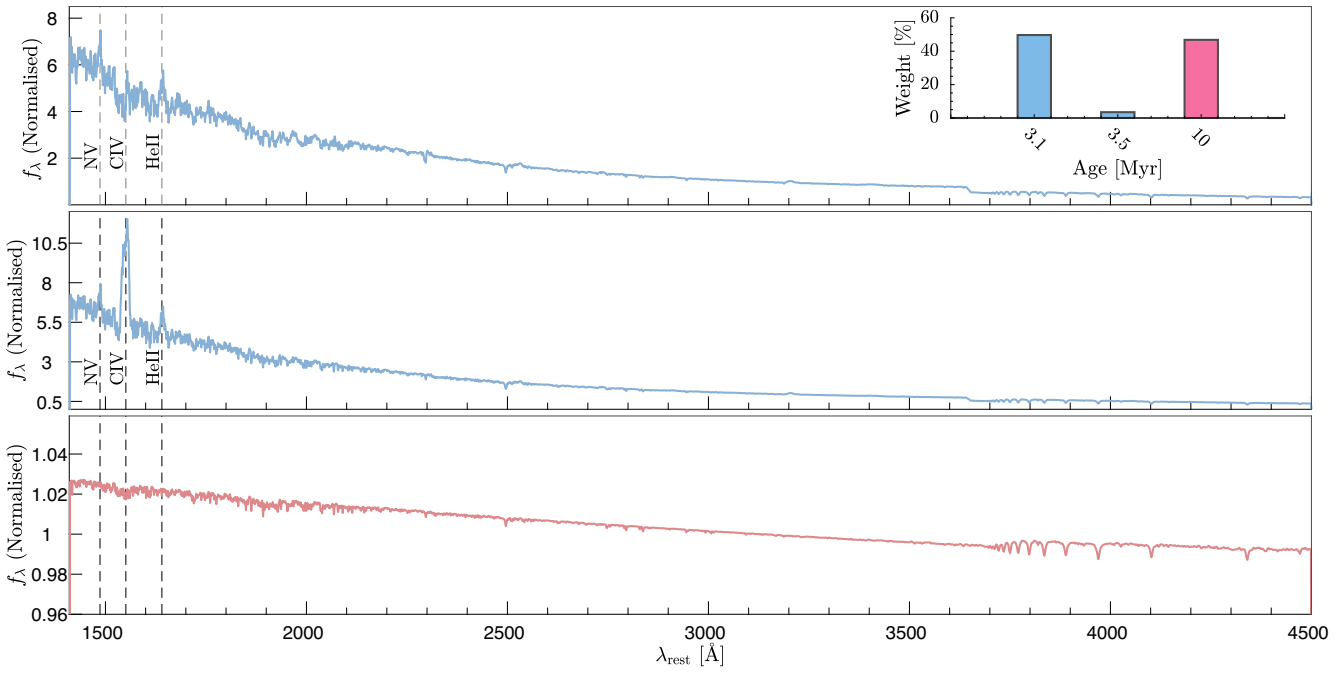

Figure 11. The lightweighted and dust-obscured individual stellar population templates contributing to the best-fitting model shown in Fig. 10. At solar metallicity, a $\sim 3.1 - 3.5$ Myr old stellar population appear to contribute >50 per cent by weight to the best-fitting model of GN-z11 (blue), and the rest by a ~ 10 Myr population (red). Also shown are the prominent carbon, helium and nitrogen broad emission peaks unique to WR stars. The inset shows the age distribution and the respective lightweights. The templates are normalized at ~ 3000 Å.

30 Myr for $Z_s = 0.5Z\odot$ and 10 Myr for $Z_s = 0.25Z\odot$. These model-derived ages are broadly consistent with the stellar population age of ∼19 Myr estimated by A. J. Bunker et al. (2023) using BEAGLE-SED fitting.

Finally, to further investigate the role of WR stars in GN-z11, we subtract the best-matching stellar and nebular continuum models for each metallicity considered and fit Gaussian profiles to the prominent emission lines (see Fig. 10) to measure their fluxes.

In the following subsections, we compare and analyse GN-z11 within the framework of various UV emission-line diagnostic schemes constructed based on the STARBURST99/PARSEC + CLOUDY library of models.

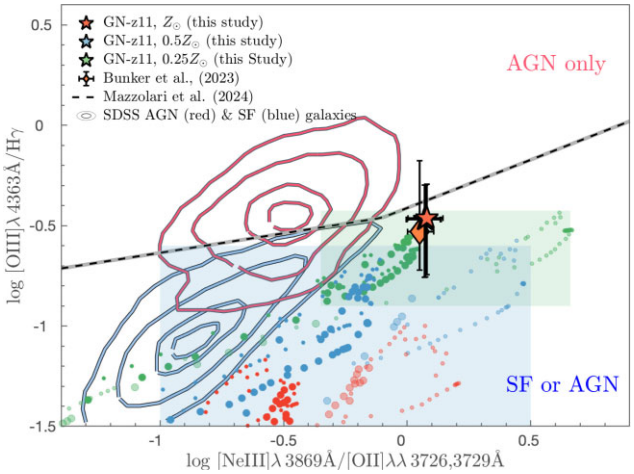

Figure 12. The new AGN diagnostics based on the [O III] λ4363 auroral line introduced by G. Mazzolari et al. (2024). the STARBURST99/PARSEC + CLOUDY predictions of the [Ne III] λ3869/[O II] λλ3726,3729 versus [O III] λ4363/Hγ line ratios used by G. Mazzolari et al. (2024) for discriminating AGNs. Similarly to previous figures, the models correspond to starbursts of strengths 10 000 and 100 000 $M_\odot$ (filled in circles with decreasing symbol sizes) with different colours representing SMC-like, LMC-like and Solar metallicities. The lighter and darker shadings of the same colour denote n_H of 100 and 1000 [cm^{-3}], respectively. The shaded regions in each panel approximately denote the parameter space sampled by SMC- and LMC-like metallicity models during the stellar population ages dominated by WR stars. Also shown are the GN-z11 measurements from A. J. Bunker et al. (2023, orange diamond) and the measurements based on this study (red, blue, and green stars) for different metallicities. The contours are reproduced from fig. 2 of G. Mazzolari et al. (2024), and denote the distributions of the SDSS AGN (red) and SF (blue) galaxies for 90 per cent, 70 per cent, 30 per cent, and 10 per cent of the populations, with the dashed black line indicating their AGN demarkation.

5.2 AGN diagnostics of GN-z11 in the ultraviolet

In Fig. 12, we present the STARBURST99/PARSEC + CLOUDY model predictions within a newly introduced UV AGN diagnostic framework of G. Mazzolari et al. (2024). They propose a novel diagnostic method based on the [O III] λ4363 auroral line in combination with [Ne III] λ3869, [O II] λλ3726,3729, and Hγ to distinguish AGN activity from star formation.

Within this framework, our models are shown for stellar populations with SMC- (green), LMC- (blue), and solar-like (red) stellar metallicities, considering starbursts of strengths 10 000 and 100 000 $M_\odot$ (filled in circles with decreasing symbol sizes) and gas densities of $n_H = 100$ and 1000 cm^{-3}. As in previous figures, shaded regions corresponding to SMC- and LMC-like metallicities (the same colour scheme) indicate the parameter space occupied during stellar evolutionary phases dominated by WR stars. The dashed line represents the AGN demarcation threshold introduced by G. Mazzolari et al. (2024), while the contours, reproduced from fig. 2 of G. Mazzolari et al. (2024), illustrate the 90 per cent, 70 per cent, 30 per cent, and 10 per cent distributions of SDSS AGN and SF galaxy populations.

The data points correspond to the measurements from A. J. Bunker et al. (2023, diamond symbol) and emission-line fluxes derived by subtracting the best-fitting stellar continuum model for each stellar metallicity considered in the present analysis (star symbols).

Notably, our starburst models exhibit a systematic offset from the SDSS distribution of SF galaxies, likely due to their design to represent the starburst-driven properties of H II regions, as well as the fact that most of the model points shown correspond to stellar evolutionary phases dominated by WR populations. Importantly, the model predictions overlap with the GN-z11 measurements derived both in this study and in A. J. Bunker et al. (2023), further supporting the potential role of WR-driven enrichment in shaping the UV emission properties of GN-z11.

5.3 Exploring stellar populations in GN-z11 through other metrics in the ultraviolet

In Fig. 13, we present several UV emission-line ratio combinations across the wavelength coverage of the GN-z11 spectrum to investigate the stellar populations and ionization conditions of GN-z11.

While certain emission lines, such as O III] λλ1661,1666, [C III], C III] λλ1907, 1909, and [Ne III] λ3869 can be readily analysed by fitting Gaussian profiles to measure their fluxes, the nebular He II λ1640 and C IV λλ1548, 1550 lines present a greater challenge due to their complex line profiles and potential contributions from multiple ionization sources.

The He II λ1640 line often comprises two components: a narrow nebular emission component and a broad stellar emission component associated with WR stars (D. Schaerer & W. D. Vacca 1998). At higher metallicities, the broad WR component becomes increasingly significant,[9] while the number of photons capable of producing nebular He II λ1640 decreases. Therefore, without accounting for WR star effects, it is difficult to disentangle the nebular and stellar contributions.

The C IV λλ1548, 1550 line doublet, on the other hand, can have strong P-Cygni profiles arising from O-star winds, significantly affecting the line profile (N. R. Walborn & R. J. Panek 1984). To account for this, we simultaneously fit the emission and absorption components of the P-Cygni profile. The WR contamination in He II λ1640 by contrast, is at least partly mitigated in our models since they incorporate WR star effects.

The resulting line flux ratios are shown as stars in each panel of Fig. 13, while the ratios reported by A. J. Bunker et al. (2023) are plotted as diamonds. The light blue and green shaded regions represent the parameter space for line ratio combinations during stellar ages dominated by WR contributions for 0.5 and 0.25$Z_\odot$ metallicities, respectively. Note also that all of these diagnostic diagrams use emission lines that are relatively close in wavelength space to minimize the effects of reddening.

In Figs 13 (a)–(c), we present diagnostics involving [C III], C III] λλ1907, 1909 to C IV λλ1548, 1550 collisionally excited line doublets and the He II λ1640 Balmer recombination line, which are commonly observed in UV galaxy spectra. The ratios [C III], C III] λλ1907, 1909 to He II λ1640 and C IV λλ1548, 1550 to He II λ1640 exhibit sensitivity to metallicity, while the combination of species from different ionization states, e.g. [C III], C III] λλ1907, 1909 to He II λ1640 and C IV λλ1548, 1550 to He II λ1640, primarily trace the ionization state (T. Nagao, R. Maiolino & A. Marconi 2006; A. Feltre et al. 2016).

Due to increasing ionization potentials from C III, to He II, to O III, to C IV (see Section 4.2), at fixed other physical parameters, the [C III], C III] λλ1907, 1909/C IV λλ1548, 1550 and [C III], C III] λλ1907, 1909/He II λ1640 ratios are expected to decrease, while the C IV λλ1548, 1550/He II λ1640, and

[9]This is because the minimum initial mass required to form a WR star decreases with increasing metallicity, allowing more stars to enter the WR phase.

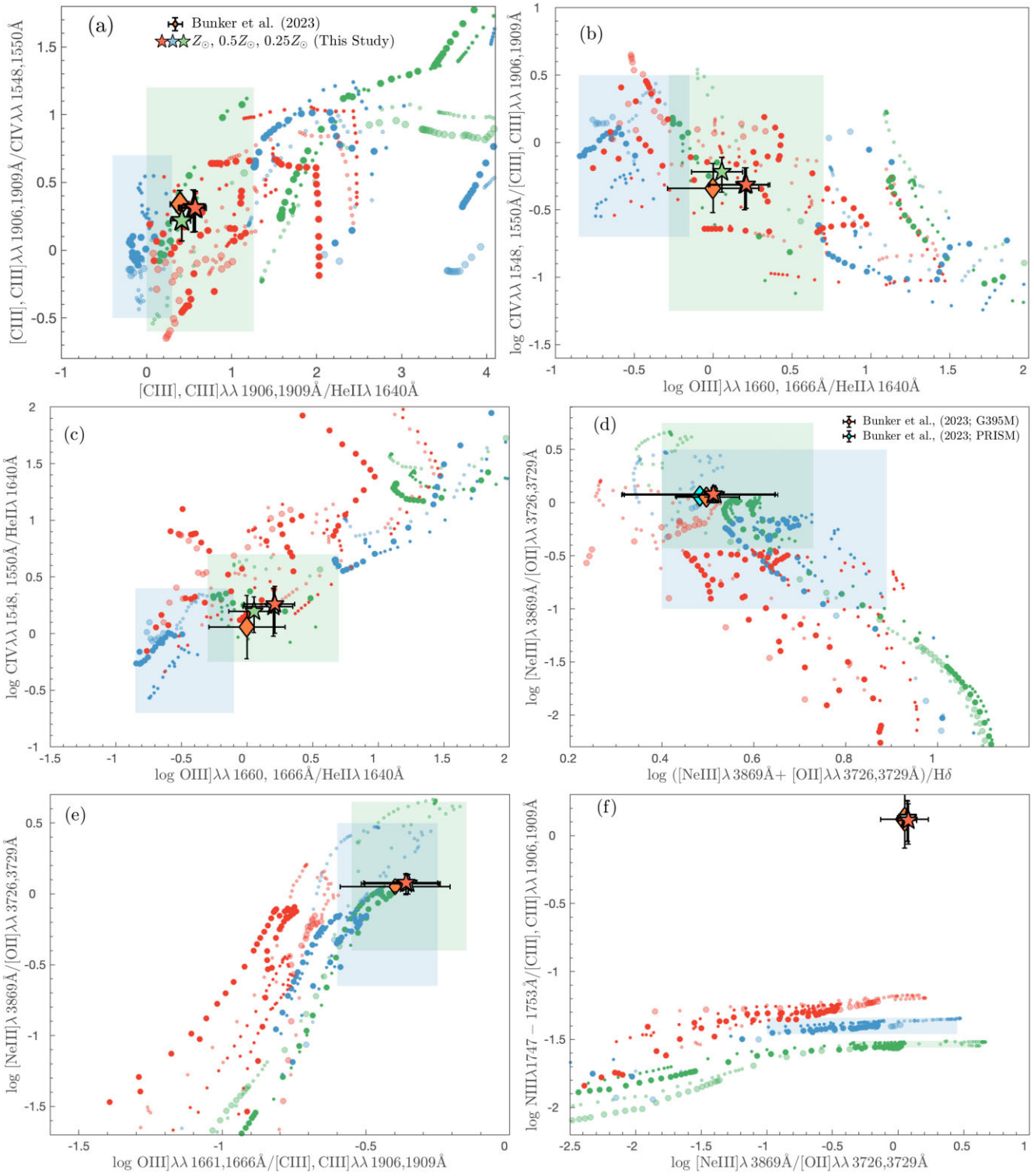

Figure 13. The UV diagnostics of prominent emission-line luminosities observed in GN-z11. (a) [C III], C III] λλ1907, 1909/C IV λλ1548, 1550 against [C III], C III] λλ1907, 1909 to He II λ1640, (b) [Ne III] λ3869/[O II] λλ3726,3729 against ([Ne III] λ3869+ [O II] λλ3726,3729)/Hδ, (c) C IV λλ1548, 1550/[C III], C III] λλ1907, 1909 against O III] λλ1661,1666/He II λ1640, (d) C IV λλ1548, 1550/He II λ1640 against O III] λλ1661,1666/He II λ1640, (e) [Ne III] λ3869/[O II] λλ3726,3729 against O III] λλ1661,1666/[C III], C III] λλ1907, 1909, and (f) N III λ1747 − 1753/[C III], C III] λλ1907, 1909 against [Ne III] λ3869/[O II] λλ3726,3729. As also described in Fig. 12, the models correspond to starbursts of strengths 10 000 and 100 000 $M_\odot$ (filled in circles with decreasing symbol sizes) with different colours representing SMC-like, LMC-like, and Solar metallicities. The lighter and darker shadings of the same colour denote n_H of 100 and 1000 cm^{-3}, respectively. The shaded regions in each panel approximately denote the parameter space sampled by SMC- and LMC-like metallicity models during the stellar population ages dominated by WR stars. Also shown are the GN-z11 measurements from A. J. Bunker et al. (2023, orange diamond) and the measurements based on this study (red, blue, and green stars) for different metallicities.

O III] λλ1661,1666/He II λ1640 ratios rise. This behaviour is clearly evident in panels (a)–(c) for stellar ages not dominated by WR stars.

During the WR phase, however, the sudden influx of ionizing photons from WR stars temporarily reverses these trends due to the increased ionization parameter. After this initial phase, the evolutionary behaviours of the line ratios generally return to the expected patterns, although fluctuations can occur due to the sequential appearance of different WR subtypes.

As noted in Section 4, we adopt a solar C/O ratio of 0.44 and ξ_d of 0.36 across all metallicities considered. Since our metallicity range is limited to values that permit WR star formation, the overall impact of these assumptions on the results shown in Fig. 13 is expected to be minimal. However, the potential effects of varying C/O and ξ_d our results are discussed below.

Variations in the C/O ratio can have a significant and direct impact on emission-line ratios involving [C III], C III] λλ1907, 1909, C IV λλ1548, 1550, and O III] λλ1661,1666. In fact, the prominence of these UV emission lines makes the line ratios based on them effective tracers of the C/O ratio in SF regions (J. Gutkin et al. 2016). For instance, J. Gutkin et al. (2016) demonstrate that increasing the C/O ratio from $0.1(\mathrm{C/O})_\odot$ to $1.4(\mathrm{C/O})_\odot$ leads to a substantial enhancement – by approximately an order of magnitude – in [C III], C III] λλ1907, 1909 and C IV λλ1548, 1550 relative to He II λ1640. In Fig. 13(a), a 40 per cent increase in the C/O ratio, for example, would result in a more pronounced enhancement of [C III], C III] λλ1907, 1909/He II λ1640 compared to [C III], C III] λλ1907, 1909/C IV λλ1548, 1550, as while both C III] and C IV lines strengthen with increasing C/O, the enhancement is greater for C III] than for C IV. On the other hand, a 40 per cent decrease in the C/O ratio would produce the opposite trend, which is likely the case given that A. J. Cameron et al. (2023) report a C/O ratio of > 0.17 for GN-z11.

Consequently, the primary shifts would be observed in the [C III], C III] λλ1907, 1909/C IV λλ1548, 1550 and C IV λλ1548, 1550/He II λ1640 ratios, shown in panels (b) and (c), respectively.

For ξ_d, the adopted value of 0.36 provides a typical balance for the metallicities considered in this analysis. However, an increase in ξ_d has a complex effect on the line ratios involving [C III], C III] λλ1907, 1909, C IV λλ1548, 1550. The depletion of coolants from the gas phase reduces cooling efficiency through infrared fine-structure transitions, leading to higher electron temperatures and enhanced cooling via optical and UV transitions (A. Feltre et al. 2016; J. Gutkin et al. 2016).

At low $Z_{\rm ISM}$, a rise in ξ_d decreases the [C III], C III] λλ1907, 1909/He II λ1640, and C IV λλ1548, 1550/He II λ1640 ratios due to the depletion of carbon from the gas phase. Conversely, at high $Z_{\rm ISM}$, increasing ξ_d enhances these ratios as the depletion of the coolants from the gas phase leads to higher electron temperatures, thus a higher excitation rate. This effect is, however, tempered to an extent by the increase in dust optical depth associated with higher ξ_d, which can lower electron temperatures through enhanced absorption of energetic photons. This interplay between coolant depletion, electron temperature, and dust absorption highlights the complex impact of ξ_d on C-species, in particular.

On the other hand, non-refractory elements, such as nitrogen and sulfur, generally show a mild increase in emission-line strengths with rising electron temperatures, as they are less affected by dust depletion and primarily respond to thermal conditions in the gas phase.

The diagnostic combinations involving neon are presented in Figs 13(d) and (e). As discussed in detail in Section 5, the [Ne III] λ3869/[O II] λλ3726,3729 versus ([Ne III] λ3869+ [O II] λλ3726,3729)/Hδ and O III] λλ1661,1666/[C III], C III] λλ1907, 1909 act to diagnose the ionization conditions, which for GN-z11, are within $-2.0 \lesssim \log U \lesssim -1.0$.

Overall, the various UV line luminosity predictions accounting for the effects of the WR phase in massive stars, shown in Figs 13(a)–(e), exhibit strong agreement with the observed line luminosity ratios reported in this study (largely consistent with the line flux measurements reported in A. J. Bunker et al. 2023). Additionally, A. J. Bunker et al. (2023) present GN-z11 observations of C III] λλ1907, 1909 to C IV λλ1548, 1550 against C III] λλ1907, 1909 to He II λ1640, alongside the models of J. Gutkin et al. (2016), highlighting a lack of models that adequately sample the parameter space hosting GN-z11 (see figs 4 and 8 of A. J. Bunker et al. 2023). We find that this discrepancy can be resolved by incorporating the evolutionary effects of WR stars.

While panels (a)–(e) of Fig. 13 show good agreement between the model predictions and the measured flux ratios of GN-z11, the N III λ1747 − 1753/O III] λλ1661,1666 ratio shown in the panel (f) exhibits a significant offset. Specifically, the models underpredict the N III/O III] ratio by more than an order of magnitude, where, our current models, incorporating WR evolution, appear insufficient to reproduce the high N III/O III] ratio observed in GN-z11.

It is, in fact, the clear presence of N IV] λλ1483, 1487 and N III] λ1747 − 1753 (A. J. Bunker et al. 2023), which are very rarely observed in the local Universe (M. Mingozzi et al. 2022, 2024), that has opened an intense debate on the physical conditions leading significantly elevated nitrogen enrichment in GN-z11 at only 440 Myr after the big bang.

Although N III] λ1747−1753 is significantly detected, the O III] λλ1661,1666 line is only marginally detected. Moreover, converting the observed N III]/O III] ratio into a total N/O abundance carries significant uncertainties due to its dependence on electron density and temperature.

Therefore, to assess the robustness of the inferred high N/O ratio in light of these uncertainties, we use PYNEB (V. Luridiana, C. Morisset & R. A. Shaw 2013) to compute emissivity over all combination of atomic parameters to explore the spread in N III] λ1747 − 1753 to O III] λλ1661,1666 ratio as a function of the electron temperature in the 5000–40 000 K range and densities in the $1–10^5$ cm^{-3} range, using the nitrogen to oxygen abundance from B. Groves et al. (2008). The resulting parameter space is illustrated in Fig. 14.

As can be seen, for a given nitrogen to oxygen scaling, the spread in line flux ratios is minimal with respect to changes in electron temperature and density, and lies far below the observed flux ratio of GN-z11. A significant scaling on N/O is in fact required to bring the PYNEB models in agreement with the observations.

However, the unusual line ratios shown in the final panel of Fig. 13 suggest an elevated N/O abundance. While the inclusion of WR stars helps to narrow the gap between the observed line luminosity ratios and model predictions, the observed level of N/O enhancement cannot be fully explained by WR stars alone. The presence of dust may contribute to an increase in the modelled N III λ1747 − 1753/[C III], C III] λλ1907, 1909 ratios, and the associated uncertainties may help narrow the gap between the models and observations. However, given the magnitude of the discrepancy, it is unlikely that dust effects alone can explain the enhanced N/O ratios either. To this end, several explanations have been proposed in the literature. For example, F. Rizzuti et al. (2025) use chemical evolutionary models with varied SFHs to show that galaxies with extreme star formation rates and differential galactic winds, where the products of core-collapse

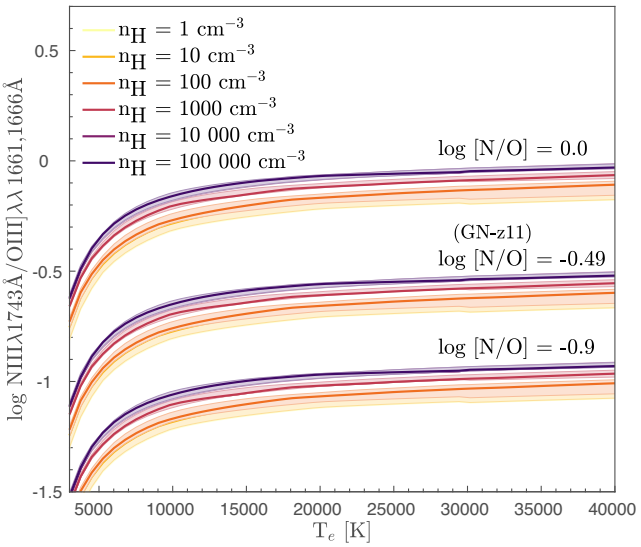

Figure 14. PYNEB analysis on the variation of N III] λ1750 multiplet to O III] λλ1661,66 doublet ratio covering all combinations of atomic parameters (i.e. energy levels, statistical weights, transition probabilities, and effective collision strengths) in a grid of density and temperature for log (N/O) values of −0.9, −0.49 (reported for GN-z11 by A. J. Cameron et al. 2023), and 0.0. The colour coding denote different densities, with each colour indicating the variation in the median N III] λ1750 multiplet to O III] λλ1661,66 ratio with increasing electron temperature. The shading of the same colour denote the 16th and 84th percentiles.

supernovae are preferentially expelled, can reproduce supersolar N/O abundances.

6 DISCUSSION

In this paper, we investigate the unusual emission-line luminosity ratios observed in the JADES NIRSpec spectroscopy of GN-z11. The JADES data reveal high line luminosities and a significant detection of the rarely observed N III] λ1748 − 1753 multiplet, suggesting an unusually high N/O abundance.

Our study is motivated by the analysis of the JADES spectrum of GN-z11 presented in A. J. Bunker et al. (2023). Their findings indicate that, based on the observed emission-line ratios and photoionization models for AGN (A. Feltre et al. 2016) and star formation (J. Gutkin et al. 2016), neither AGN activity nor star formation alone can explain GN-z11's position in the C III]/He II versus C III]/C IV diagnostic plane (see fig. 4 of A. J. Bunker et al. 2023). Furthermore, using the ([Ne III] + [O II])/Hδ versus [Ne III]/[O II] diagnostic ratios, A. J. Bunker et al. (2023) report a metallicity range of $0.07 \lesssim Z/Z_{\odot} \lesssim 0.15$ and an ionization parameter, log, $U \sim -2$, for GN-z11.

Building on the findings of A. J. Bunker et al. (2023), we develop a suite of stellar and nebular models to further investigate the nature of the stellar populations in GN-z11, utilizing the STARBURST99 SPS and CLOUDY photoionization codes. The intense emission-line luminosities observed in the spectrum of GN-z11 suggest that the galaxy is undergoing an extreme starburst event. Therefore, our objective, in particular, is to explore whether incorporating the WR evolutionary phase of massive stars can resolve the discrepancies reported in A. J. Bunker et al. (2023).

To achieve this, we modify and update STARBURST99 to incorporate high-resolution stellar spectral libraries, with a particular focus on accurately modelling the WR evolutionary phases of massive stars, as detailed in Section 3. The resulting stellar population models are then used as inputs for CLOUDY, enabling the self-consistent generation of nebular models across metallicities that support WR star formation (Section 4).

The equivalent of figs 4 and 8 from A. J. Bunker et al. (2023), reconstructed using the models developed in this study, are presented in Figs 8 and 9, respectively. As shown in Fig. 8, our starburst models, incorporating improvements to the WR evolutionary phase of massive stars, successfully sample the parameter space occupied by GN-z11. Importantly, we find that the emergence of WR stars is essential to produce a sufficient fraction of ionizing photons to populate the region of the C III]/He II versus C III]/C IV nebular line diagnostic plane where GN-z11 resides – a region notably lacking in models in fig. 4 of A. J. Bunker et al. (2023).

Using the metallicity-sensitive ([Ne III] + [O II])/Hδ versus [Ne III]/[O II] diagnostic, A. J. Bunker et al. (2023) estimate a metallicity range of $0.07 \lesssim Z/Z_{\odot} \lesssim 0.15$ for GN-z11 (see their fig. 8). This metallicity estimate and their assessment of log $U \approx -2$ are in agreement with our model-based derivations.

In the remainder of this paper, we build on the analysis of A. J. Bunker et al. (2023) to further investigate the properties of the underlying stellar populations of GN-z11. Fig. 13 presents different UV emission-line diagnostics considered in this study. The observed line flux ratios shown represent the emission-line luminosities derived as a part of this study from subtracting the best-fitting continuum model of each stellar metallicity capable of supporting WR star formation (e.g. see Fig. 10 for the best-fitting continuum model for $Z_s = Z_{\odot}$) alongside the A. J. Bunker et al. (2023) measurements.

Overall, the model diagnostics presented in Figs 13(a)–(e) align well with the observed line luminosities measured in this study, which are consistent with those reported by A. J. Bunker et al. (2023) when accounting for the effects of the WR phase in massive stars.

In addition to the PARSEC models, we employed the GENEVA stellar evolutionary tracks for comparison with the PARSEC models. Overall, massive stars tend to enter the WR phase earlier in the GENEVA models, yielding slightly younger best-fitting ages than those derived using PARSEC. This discrepancy is likely driven by the higher mass-loss rates assumed for massive stars in the GENEVA framework, which accelerates their evolutionary progression. Minor differences are also apparent in the predicted emission-line ratios, with adjustments in $n_{\rm H}$, stellar metallicity, and burst strengths required to achieve similar sampling. These variations likely arise primarily from differences in the treatment of mass loss, along with other model-dependent assumptions. Despite these discrepancies, the GENEVA predictions are broadly consistent with those of PARSEC. Note that, while we have not explicitly modelled stochastic effects in this study, previous work by R. Arora et al. (2021) and R. Orozco-Duarte et al. (2022) demonstrates that stochastic sampling introduces significant dispersion around individual points along model tracks. Within the context of our analysis, such stochastic effects effectively broaden the parameter space spanned by the tracks, thereby further enhancing their ability to reproduce the observed properties of GN-z11.

Part of the puzzle of stellar populations in GN-z11, however, remains unsolved as the PARSEC or GENEVA models cannot reproduce the notable underestimate of N III]/O III] shown in Fig. 13(f). The unusual line ratios suggest an elevated N/O abundance. While the presence of WR stars partially bridges the gap between the observed line luminosity ratios and the model predictions, the observed magnitude of the N/O enhancement cannot be fully explained by WR stars alone.

To investigate this further, taking into account the dependence of N and O on temperature and density, we examined the emissivities of N III] and O III] over all combinations of atomic parameters to explore the spread in N III] λ1747 − 1753/O III] $\lambda\lambda$1661,1666 ratio in electron temperature and density space (Fig. 14). For reference, the log(N/O) ratio of −0.49 reported by A. J. Cameron et al. (2023) for GN-z11, which is approximately twice the solar value of log(N/O) = −0.86 (M. Asplund et al. 2009), is also indicated in Fig. 14. These results suggest that a significant scaling of N/O is required to bring the observed line ratios into agreement with the model predictions.

As discussed earlier, several explanations have been proposed in the literature to account for elevated N/O abundances. For example, F. Rizzuti et al. (2025) use chemical evolution models incorporating a range of SFHs to show that galaxies with intense star formation and differential galactic winds, where core-collapse supernova ejecta are preferentially removed, can achieve supersolar N/O ratios. A. J. Cameron et al. (2023) explore multiple scenarios, including enrichment from WR stars, runaway stellar collisions in dense clusters forming very massive stars, and tidal disruption events, as possible mechanisms for nitrogen enhancement. A similar pathway involving massive stars is proposed by J. S. Vink (2024), while K. Watanabe et al. (2024) suggest that nitrogen-rich winds from rotating WR stars that undergo direct collapse could also play a role (see Introduction for further discussion).

Interestingly, T. Tapia, K. Bekki & B. Groves (2024) argue for the complete absence of WR stars in the stellar populations of GN-z11. Their conclusion is based on chemical evolution modelling aimed at reproducing the elemental abundance patterns observed in the Sunburst Arc cluster. Similar to GN-z11, the Sunburst Arc exhibits elevated N/O and suppressed C/O abundance ratios (e.g. log C/O $\sim$ −0.78 for GN-z11; A. J. Cameron et al. 2023), making it a suitable lower redshift ($z \sim 2.24$) analogue for studying chemically enriched systems at high redshift.

Using the chemical evolution models of M. Limongi & A. Chieffi (2018), T. Tapia et al. (2024) find that the observed abundance patterns are best reproduced when WR stars are excluded, as their presence would enhance the C/O ratio. Instead, their models invoke enrichment from OB stars via stellar winds and core-collapse supernovae, under the assumption that the most massive stars ($M > 25$ $M_\odot$) collapse directly into black holes at the end of their lifetimes, thus bypassing the WR phase. The recent *JWST* observations by T. E. Rivera-Thorsen et al. (2024), however, reveal a population of WR stars in the Sunburst Arc cluster, suggesting that these stars may contribute to rapid local nitrogen enrichment, contrary to the assumptions of T. Tapia et al. (2024).

While T. Tapia et al. (2024) offer one plausible explanation for the elevated N/O abundance observed in GN-z11, several alternative scenarios, also merit consideration. An important consideration is that not all WR subtypes contribute equally to the enrichment of nitrogen and carbon, the resulting abundance ratios depend on the relative fractions of WN and WC subtypes. WN stars, in particular, can significantly enhance N/O without substantially affecting C/O (e.g. J. Brinchmann et al. 2008b; Y. Zhang, T. Morishita & M. Stiavelli 2025). For example, to explain the unusually high N/O abundances observed in a $z \sim 4.69$ SF galaxy, Y. Zhang et al. (2025) propose a scenario in which massive WR stars ($M > 25$ $M_\odot$) collapse directly into black holes, enriching the surrounding medium in nitrogen. This scenario appears to be conceptually similar to that of T. Tapia et al. (2024), with the key distinction being that the stars are allowed to evolve through a WR phase prior to collapse.

Moreover, observations of WR galaxies reveal considerable variation in WN-to-WC ratios. For instance, the low-metallicity dwarf WR galaxy I ZW 18 exhibits an unexpectedly high WC-to-WN ratio (V. Lebouteiller et al. 2013), a trend atypical for its metallicity. In fact, the work of M. A. Peña-Guerrero et al. (2017) demonstrates that the C/N versus metallicity relation in WR galaxies shows wide scatter, although, the overall tendency is toward higher WC-to-WN ratios with increasing metallicity.

The predicted abundance patterns are also sensitive to the specific implementation of WR stars in stellar population models. For example, the models used by T. Tapia et al. (2024), based on M. Limongi & A. Chieffi (2018), predict a relatively high fraction of WNE and WC stars compared to WNL stars at solar metallicity, in contrasts with observations in the MW, where WNL stars are more prevalent than WNE (G. Meynet & A. Maeder 2005). Similarly, in our models at solar metallicity, WNL stars dominate over WNE and WC subtypes, and at certain stellar population ages, WC stars are absent altogether. These differences in WR subtype distributions can have a significant impact on the predicted abundance of N/O versus C/O abundance ratios.

Taken together, both the wide variation observed in WR galaxies and the uncertainties in model implementations methodologies suggest that the presence of WR stars, such as those observed in the Sunburst Arc, can be interpreted in different ways. In particular, models that do not produce large WC populations can still be consistent with the observed high N/O abundances without necessarily predicting a strong increase in C/O. A discussion of how different diagnostics respond to variations in the C/O ratio within our models is provided in Section 5.3.

Therefore, it is plausible that the enrichment observed in GN-z11 arises from a combination of these processes. For instance, incorporating higher wind velocities for stars entering the WR phase in our models could help reconcile the predicted and observed line ratios associated with nitrogen.

7 SUMMARY

In this study, we analyse the JADES NIRSpec spectrum of GN-z11, which reveals high emission-line luminosities and a significant detection of the rarely observed N III] λ1748 − 1753 multiplet, suggesting an unusually high N/O abundance.

Our stellar and nebular models, developed using STARBURST99 and CLOUDY, demonstrate that the WR evolutionary phase of massive stars plays a crucial role in explaining the strong ionizing radiation and emission-line ratios. The inclusion of WR stars allows our models to reproduce GN-z11's position in the C III]/He II versus C III]/C IV diagnostic plane, which was not fully explained by previous models.

Moreover, our model-based metallicity and ionization parameter estimates ($0.07 \lesssim Z/Z_\odot \lesssim 0.15$, $\log, U \approx -2$) are in agreement with those derived in A. J. Bunker et al. (2023). Likewise, the stellar ages inferred from our model fitting are in good agreement with the SED-based age of $\sim$ 19 Myr presented in their study.

We find that while WR stars contribute significantly to the observed line ratios and are able to explain the position of GN-z11 in various diagnostic diagrams, they alone cannot fully explain the unusually high N III]/O III] ratio. This suggests that an additional mechanism is required to enhance the N/O abundance in GN-z11.

AUTHOR CONTRIBUTION STATEMENT

MLPG devised the project, carried out the analysis, and drafted the paper. MLPG and JB contributed to the data analysis. MLPG, JB, SC, and AJB contributed to the interpretation of the results. All authors discussed the results and commented on the manuscript.

ACKNOWLEDGEMENTS

We thank Caroline Foster for the initial discussions on analysis and the presentation of the paper. This research was supported by the Australian Research Council Centre of Excellence for All Sky Astrophysics in 3 Dimensions (ASTRO3D, CE170100013), and the Australian Research Council (ARC) grant DP190102714. JB acknowledges support from Fundação para a Ciência e a Tecnologia (FCT) through the research grants UIDB/04434/2020 and UIDP/04434/2020. DOI: 10.54499/UIDB/04434/2020 and DOI: 10.54499/UIDP/04434/2020. 2020.03379.CEECIND/CP1631/CT0003 and DOI: 10.54499/2020.03379.CEECIND/CP1631/CT0003. AJB acknowledges funding from the 'FirstGalaxies' Advanced Grant from the European Research Council (ERC) under the European Union's Horizon 2020 research and innovation program (grant agreement no. 789056). SO acknowledges support from the National Research Foundation (NRF) grant funded by the Korea government (MSIT) (RS-2023-00214057 and RS-2025-00514475). This study uses the ⟨0:sc ⟩python⟨/0:sc⟩ programming language. We acknowledge the use of NUMPY (C. R. Harris et al. 2020), SCIPY (P. Virtanen et al. 2020), MATPLOTLIB (J. D. Hunter 2007), ASTROPY (Astropy Collaboration 2018, 2022), and TOPCAT (M. B. Taylor 2005).

DATA AVAILABILITY

This analysis is conducted using the data and emission-line fluxes presented in A. J. Bunker et al. (2023).

REFERENCES

Allen M. G., Dopita M. A., Tsvetanov Z. I., 1998, ApJ, 493, 571
Álvarez-Márquez J. et al., 2025, A&A, 695, A250
Arora R., Krumholz M. R., Federrath C., 2021, MNRAS, 508, 3290
Asplund M., Grevesse N., Sauval A. J., Scott P., 2009, ARA&A, 47, 481
Astropy Collaboration, 2018, AJ, 156, 123
Astropy Collaboration, 2022, ApJ, 935, 167
Baldwin J. A., Phillips M. M., Terlevich R., 1981, PASP, 93, 5
Bestenlehner J. M. et al., 2025, A&A, 695, A198
Bouwens R. J. et al., 2010, ApJ, 725, 1587
Bressan A., Marigo P., Girardi L., Salasnich B., Dal Cero C., Rubele S., Nanni A., 2012, MNRAS, 427, 127
Brinchmann J., Charlot S., White S. D. M., Tremonti C., Kauffmann G., Heckman T., Brinkmann J., 2004, MNRAS, 351, 1151
Brinchmann J., Kunth D., Durret F., 2008b, A&A, 485, 657
Brinchmann J., Pettini M., Charlot S., 2008a, MNRAS, 385, 769
Bruzual G., Charlot S., 2003, MNRAS, 344, 1000
Bunker A. J. et al., 2023, A&A, 677, A88
Byler N., Dalcanton J. J., Conroy C., Johnson B. D., 2017, ApJ, 840, 44
Byrne C. M., Stanway E. R., 2023, MNRAS, 521, 4995
Calzetti D., Armus L., Bohlin R. C., Kinney A. L., Koornneef J., Storchi-Bergmann T., 2000, ApJ, 533, 682
Cameron A. J. et al., 2023, A&A, 677, A115
Chandar R., Leitherer C., Tremonti C. A., 2004, ApJ, 604, 153
Charbonnel C., Meynet G., Maeder A., Schaller G., Schaerer D., 1993, A&AS, 101, 415
Charlot S., Fall S. M., 2000, ApJ, 539, 718
Chatzikos M. et al., 2023, Rev. Mex. Astron. Astrofis., 59, 327
Chen Y., Bressan A., Girardi L., Marigo P., Kong X., Lanza A., 2015, MNRAS, 452, 1068
Chen Y., Girardi L., Bressan A., Marigo P., Barbieri M., Kong X., 2014, MNRAS, 444, 2525
Choi J., Dotter A., Conroy C., Cantiello M., Paxton B., Johnson B. D., 2016, ApJ, 823, 102
Coelho P., Bruzual G., Charlot S., Weiss A., Barbuy B., Ferguson J. W., 2007, MNRAS, 382, 498
Crowther P. A., 2007, ARA&A, 45, 177
Crowther P. A., Dessart L., Hillier D. J., Abbott J. B., Fullerton A. W., 2002, A&A, 392, 653
Cunha K., Hubeny I., Lanz T., 2006, ApJ, 647, L143
de Jager C., Nieuwenhuijzen H., van der Hucht K. A., 1988, A&AS, 72, 259
Dessart L., Crowther P. A., Hillier D. J., Willis A. J., Morris P. W., van der Hucht K. A., 2000, MNRAS, 315, 407
Dopita M. A., Groves B. A., Sutherland R. S., Binette L., Cecil G., 2002, ApJ, 572, 753
Dopita M. A., Kewley L. J., Heisler C. A., Sutherland R. S., 2000, ApJ, 542, 224
Doran E. I. et al., 2013, A&A, 558, A134
Efstathiou A., Rowan-Robinson M., Siebenmorgen R., 2000, MNRAS, 313, 734
Ekström S. et al., 2012, A&A, 537, A146
Eldridge J. J., Stanway E. R., 2009, MNRAS, 400, 1019
Eldridge J. J., Stanway E. R., Xiao L., McClelland L. A. S., Taylor G., Ng M., Greis S. M. L., Bray J. C., 2017, Publ. Astron. Soc. Aust., 34, e058
Feltre A., Charlot S., Gutkin J., 2016, MNRAS, 456, 3354
Ferland G. J. et al., 2013, Rev. Mex. Astron. Astrofis., 49, 137
Ferruit P. et al., 2022, A&A, 661, A81
Georgy C., Ekström S., Hirschi R., Meynet G., Groh J. H., Eggenberger P., 2015, in Hamann W.-R., Sander A., Todt H. eds, Wolf-Rayet Stars: Proceedings of an International Workshop held in Potsdam, Germany, 1–5 June 2015, p. 229
Georgy C., Ekström S., Meynet G., Massey P., Levesque E. M., Hirschi R., Eggenberger P., Maeder A., 2012, A&A, 542, A29
Gomes J. M., Papaderos P., 2017, A&A, 603, A63
Götberg Y., de Mink S. E., Groh J. H., Leitherer C., Norman C., 2019, A&A, 629, A134
Gräfener G., Koesterke L., Hamann W.-R., 2002, A&A, 387, 244
Gräfener G., Owocki S. P., Grassitelli L., Langer N., 2017, A&A, 608, A34
Grassitelli L., Langer N., Grin N. J., Mackey J., Bestenlehner J. M., Gräfener G., 2018, A&A, 614, A86
Grevesse N., Sauval A. J., 1998, Space Sci. Rev., 85, 161
Groves B. A., Dopita M. A., Sutherland R. S., 2004, ApJS, 153, 9
Groves B., Dopita M. A., Sutherland R. S., Kewley L. J., Fischera J., Leitherer C., Brandl B., van Breugel W., 2008, ApJS, 176, 438
Gunawardhana M. L. P. et al., 2020, MNRAS, 497, 3860
Gutkin J., Charlot S., Bruzual G., 2016, MNRAS, 462, 1757
Hainich R. et al., 2014, A&A, 565, A27
Hamann W.-R., Gräfener G., 2004, A&A, 427, 697
Harris C. R. et al., 2020, Nature, 585, 357
Hillier D. J., 1991, A&A, 247, 455
Hillier D. J., Miller D. L., 1998, ApJ, 496, 407
Hunter J. D., 2007, Comput. Sci. Eng., 9, 90
Ji X. et al., 2025, MNRAS, 541, 2134
Kauffmann G. et al., 2003, MNRAS, 346, 1055
Kewley L. J., Dopita M. A., Sutherland R. S., Heisler C. A., Trevena J., 2001, ApJ, 556, 121
Kobayashi C., Ferrara A., 2024, ApJ, 962, L6
Kroupa P., 2001, MNRAS, 322, 231
Kurucz R. L., 1992, in Barbuy B., Renzini A. eds, IAU Symp. Vol. 149, The Stellar Populations of Galaxies, p. 225
Kurucz R., 1993, SYNTHE Spectrum Synthesis Programs and Line Data. Kurucz CD-ROM No. 18. Smithsonian Astrophysical Observatory, Cambridge, MA, p. 18
Langer N., 1989, A&A, 210, 93
Lanz T., Hubeny I., 2003, ApJS, 146, 417
Lebouteiller V., Heap S., Hubeny I., Kunth D., 2013, A&A, 553, A16
Leitherer C. et al., 1999, ApJS, 123, 3
Leitherer C., Ekström S., Meynet G., Schaerer D., Agienko K. B., Levesque E. M., 2014, ApJS, 212, 14
Leitherer C., Ortiz Otálvaro P. A., Bresolin F., Kudritzki R.-P., Lo Faro B., Pauldrach A. W. A., Pettini M., Rix S. A., 2010, ApJS, 189, 309
Leitherer C., Tremonti C. A., Heckman T. M., Calzetti D., 2011, AJ, 141, 37

Levesque E. M., Kewley L. J., Larson K. L., 2010, AJ, 139, 712
Levesque E. M., Richardson M. L. A., 2014, ApJ, 780, 100
Limongi M., Chieffi A., 2018, ApJS, 237, 13
Luridiana V., Morisset C., Shaw R. A., 2013, Astrophysics Source Code Library, record ascl:1304.021
Maeder A., 1990, A&AS, 84, 139
Maiolino R. et al., 2024, Nature, 627, 59
Mazzolari G. et al., 2024, A&A, 691, A345
Meynet G., 1995, A&A, 298, 767
Meynet G., Maeder A., 2005, A&A, 429, 581
Meynet G., Maeder A., Schaller G., Schaerer D., Charbonnel C., 1994, A&AS, 103, 97
Mingozzi M. et al., 2022, ApJ, 939, 110
Mingozzi M. et al., 2024, ApJ, 962, 95
Moffat A. F. J., Drissen L., Lamontagne R., Robert C., 1988, ApJ, 334, 1038
Munari U., Sordo R., Castelli F., Zwitter T., 2005, A&A, 442, 1127
Nagao T., Maiolino R., Marconi A., 2006, A&A, 459, 85
Nagele C., Umeda H., 2023, ApJ, 949, L16
Oesch P. A. et al., 2016, ApJ, 819, 129
Orozco-Duarte R. et al., 2022, MNRAS, 509, 522
Pacifici C. et al., 2023, ApJ, 944, 141
Paxton B. et al., 2013, ApJS, 208, 4
Peña-Guerrero M. A., Leitherer C., de Mink S., Wofford A., Kewley L., 2017, ApJ, 847, 107
Pérez-Montero E., Hägele G. F., Contini T., Díaz Á. I., 2007, MNRAS, 381, 125
Prevot M. L., Lequeux J., Maurice E., Prevot L., Rocca-Volmerange B., 1984, A&A, 132, 389
Rivera-Thorsen T. E. et al., 2024, A&A, 690, A269
Rizzuti F., Matteucci F., Molaro P., Cescutti G., Maiolino R., 2025, A&A, 697, A96
Rodríguez-Merino L. H., Chavez M., Bertone E., Buzzoni A., 2005, ApJ, 626, 411
Sander A. A. C., Vink J. S., Hamann W. R., 2020, MNRAS, 491, 4406
Sander A., Hamann W.-R., Todt H., 2012, A&A, 540, A144
Schaerer D., Vacca W. D., 1998, ApJ, 497, 618
Schaller G., Schaerer D., Meynet G., Maeder A., 1992, A&AS, 96, 269
Schmutz W., Hamann W. R., Wessolowski U., 1989, A&A, 210, 236
Schmutz W., Leitherer C., Gruenwald R., 1992, PASP, 104, 1164
Scholtz J. et al., 2024, A&A, 687, A283
Senchyna P., Plat A., Stark D. P., Rudie G. C., Berg D., Charlot S., James B. L., Mingozzi M., 2024, ApJ, 966, 92
Siebenmorgen R., Krügel E., 2007, A&A, 461, 445
Smith L. J., Norris R. P. F., Crowther P. A., 2002, MNRAS, 337, 1309
Stark D. P. et al., 2014, MNRAS, 445, 3200
Stark D. P. et al., 2015, MNRAS, 454, 1393
Steidel C. C. et al., 2014, ApJ, 795, 165
Tang J., Bressan A., Rosenfield P., Slemer A., Marigo P., Girardi L., Bianchi L., 2014, MNRAS, 445, 4287
Tapia T., Bekki K., Groves B., 2024, MNRAS, 534, 2086
Taylor M. B., 2005, ASPC, 347, 29
Todt H., Sander A., Hainich R., Hamann W.-R., Quade M., Shenar T., 2015, A&A, 579, A75
Tramper F., Sana H., de Koter A., 2016, ApJ, 833, 133
Tremonti C. A. et al., 2004, ApJ, 613, 898
van der Tak F. S., Lique F., Faure A., Black J. H., van Dishoeck E. F., 2020, Atoms, 8, 15
Vazdekis A., Ricciardelli E., Cenarro A. J., Rivero-González J. G., Díaz-García L. A., Falcón-Barroso J., 2012, MNRAS, 424, 157
Vázquez G. A., Leitherer C., Schaerer D., Meynet G., Maeder A., 2007, ApJ, 663, 995
Villar-Martin M., Tadhunter C., Clark N., 1997, A&A, 323, 21
Vink J. S. et al., 2023, A&A, 675, A154
Vink J. S., 2024, preprint (arXiv:2410.18980)
Virtanen P. et al., 2020, Nat. Methods, 17, 261
Walborn N. R., Panek R. J., 1984, ApJ, 286, 718
Watanabe K. et al., 2024, ApJ, 962, 50
Zhang Y., Morishita T., Stiavelli M., 2025, preprint (arXiv:2502.04817)

APPENDIX A: COMPARISON OF STARBURST99 MODELS WITH CHARLOT & BRUZUAL (2019)

To investigate the role of WR stars in explaining the observed properties of GN-z11, we have developed our own set of stellar population models. This approach provides the necessary flexibility to systematically explore various prescriptions for WR evolution, assess the influence of WR stars on the overall population, and trace the time-dependent behaviour of the stellar population at high spectral and temporal resolution, particularly during the brief evolutionary phases when WR features are most prominent.

While this tailored modelling framework is needed for addressing our specific scientific goals, it is important to compare our models against established frameworks in the literature, such as those of Charlot & Bruzual (G. Bruzual & S. Charlot 2003, see also footnote[6] for the link to the latest models), which serve as a valuable reference baseline.

In Fig. A1, we compare our models (black lines), previously shown and described in Fig. 5 and Section 4.2, with the 2019 release of the Charlot & Bruzual models.

Qualitatively, both model sets exhibit similar time-dependent behaviour. There are, however, quantitative differences. Like our implementation, the 2019 release of the Charlot & Bruzual models incorporate the PARSEC stellar evolutionary tracks from A. Bressan et al. (2012) and Y. Chen et al. (2015), and UV spectral libraries from T. Lanz & I. Hubeny (2003), W.-R. Hamann & G. Gräfener (2004), L. H. Rodríguez-Merino et al. (2005), and C. Leitherer et al. (2010). Despite these common ingredients, discrepancies are likely arising from differing metallicity assumptions for the solar, LMC, and SMC, as well as variations in the methodologies used to link WR stellar atmospheres with the underlying stellar evolutionary models.

The behaviour of the He^0/H^0 ionizing luminosity in Fig. A1(a) is broadly similar between the two model sets at young ages, with differences emerging primarily during periods when the ionizing flux drops, which are largely outside the observable range. Relatively more substantial differences are seen in the evolution of He^+/H^0 (Fig. A1b). Nevertheless, these discrepancies generally occur over comparable age ranges and with similar magnitudes, and are therefore unlikely to introduce significant variations in the predicted emission-line results.

Furthermore, as our analysis involves fitting stellar population templates to GN-z11 in order to recover the likely underlying stellar continuum, we require templates at a resolution matched to the *JWST* spectra. This higher resolution is provided by our template set, enabling better continuum fitting.

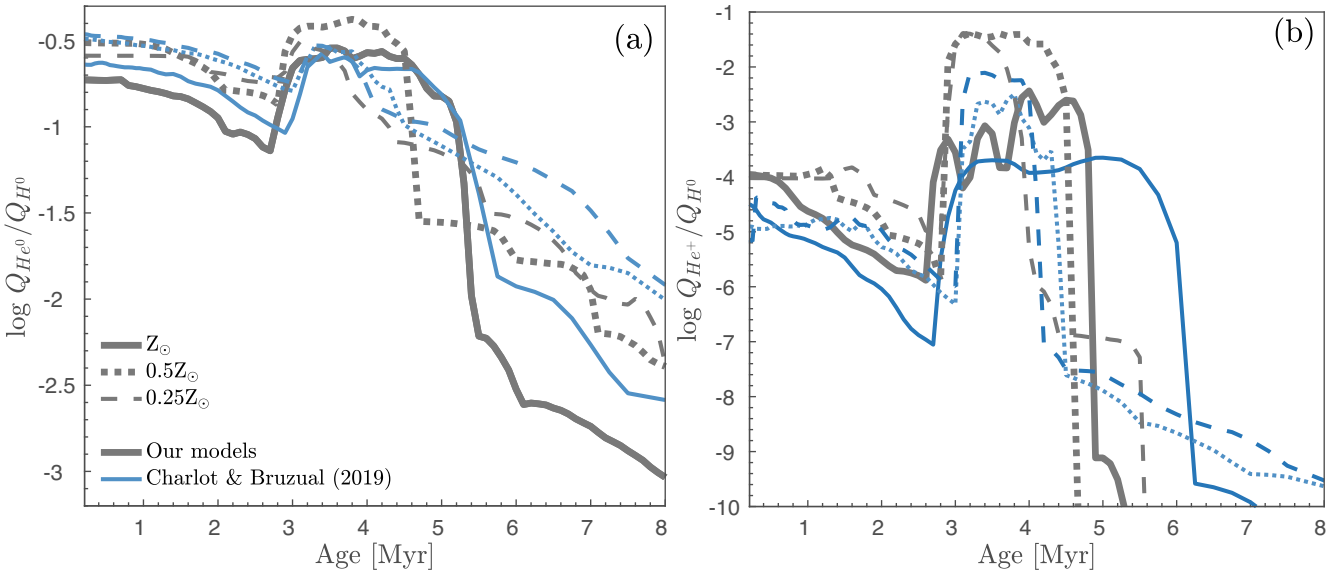

Figure A1. Comparing our models with the 2019 release of the Charlot & Bruzual models (G. Bruzual & S. Charlot 2003). The black solid, dashed, and dotted lines correspond to our models, as shown in Fig. 5, while the blue lines represent the Charlot & Bruzual (2019) models.

This paper has been typeset from a TEX/LATEX file prepared by the author.